

Application of Microwave Imaging for Brain Diagnostics

Marija Nikolic Stevanovic, Darko Ninkovic, Tushar Singh, Branislav Ninkovic, Miodrag Tasic, and Branko Kolundzija

Abstract— We present the application of the distorted Born iterative method for permittivity estimation of a realistic human phantom, which is an essential step in microwave medical diagnostics. Permittivity reconstruction is a difficult task due to the complexity of the electromagnetic model and the ill-posedness of the inverse scattering problems. Assuming that prior knowledge of the head anatomy is available from other imaging modalities, such as magnetic resonance imaging, we showed that electromagnetic tissue parameters could be accurately estimated even for tissues deeply located in the head. In our implementation of DBIM, we have gradually improved the estimation accuracy by initializing more complex models with results obtained for simpler models.

Index Terms—Microwave imaging, inverse scattering, distorted Born iterative method, human phantoms.

I. INTRODUCTION

In the last decade, the application of microwaves in medical diagnostics has gained much attention. The advantages of medical microwave imaging (MMWI) are non-invasiveness, low cost, utilization of nonionizing radiation, and ease of portability. However, due to the relatively low resolution of MMWI, it is envisioned primarily as a complementary screening tool for medical applications [1]–[3].

The gold standards in medical diagnostics are magnetic resonance imaging (MRI), computed tomography (CT), and positron emission tomography (PET) [4], [5], which produce high-resolution images with well-resolved tissues. However, their application is usually limited to large medical centers due to their high cost, and they are not appropriate for bedside monitoring. Additionally, CT and PET scans utilize harmful ionizing radiation.

The essential elements of any MMWI system are an antenna array, a reconstruction algorithm based on inverse scattering, and a reliable efficient 3D electromagnetic solver. Additionally, realistic human models (phantoms) are

M. Nikolic Stevanovic is with the School of Electrical Engineering, University of Belgrade, Serbia (e-mail: mnikolic@etf.bg.ac.rs).

D. Ninkovic is with the School of Electrical Engineering, University of Belgrade, Serbia (e-mail: darko@etf.bg.ac.rs).

T. Singh is with WIPL-D d.o.o. Belgrade, Serbia and the School of Electrical Engineering, University of Belgrade, Serbia (e-mail: tushar.singh@wipl-d.com).

B. Ninkovic is with WIPL-D d.o.o. Belgrade, Serbia (e-mail: branislav.ninkovic@wipl-d.com).

M. Tasic is with the School of Electrical Engineering, University of Belgrade, Serbia (e-mail: tasic@etf.bg.ac.rs).

B. Kolundzija is with WIPL-D d.o.o. Belgrade, Serbia and School of Electrical Engineering, University of Belgrade, Serbia (e-mail: branko.kolundzija@wipl-d.com).

necessary for designing and testing MMWI systems.

Microwave imaging algorithms are generally classified into two categories: qualitative and quantitative. The goal of qualitative algorithms in medical imaging is to detect possible lesions or other tissues changes between measurements. They cannot infer the electromagnetic properties of the changes; instead, they estimate their location and shape. Examples of qualitative imaging algorithms are truncated singular value decomposition (TSVD) [6] and the linear sampling method (LSM) [7]. In contrast, quantitative algorithms reconstruct the complex permittivity in the whole domain of interest. Since different tissues have different electromagnetic properties, permittivity maps are also images of particular body parts.

Solving quantitative algorithms is difficult due to the complex scattering phenomenon. They are non-linear and ill-posed, making them prone to false solutions and more computationally intensive than qualitative algorithms. Examples are the inexact Newton methods [8] and the distorted Born iterative method (DBIM) [9], [10].

In this paper, we study the application of the DBIM to the permittivity reconstruction of a realistic head phantom. Although the utilized method is well-established, there are only a few examples of its application to realistic 3D human models. The main reasons for this are the non-uniqueness of the solution, the lack of detailed anatomical models adapted for electromagnetic analysis, and the extremely long computational time. The goal of this work is to test the algorithm's ability to estimate tissues' permittivities. Thus, we assume that the tissue boundaries are available, e.g., from a prior MRI screening. To initialize the algorithm, we first compute the average permittivity of the head.

The paper is organized as follows. After the introduction, we explain the DBIM in Section II. Section III describes the numerical examples and presents the obtained results. Finally, in the concluding section, we summarize the obtained results and give guidelines for future work.

II. DISTORTED BORN ITERATIVE METHOD

The goal of quantitative microwave imaging is to estimate the complex permittivity of the unknown object or the whole domain of interest. Fig. 1 illustrates a three-dimensional (3D) microwave imaging scenario consisting of an unknown non-magnetic inhomogeneous object, which occupies a volume v' and has the permittivity ϵ . The object is located in a known non-magnetic background medium whose permittivity is ϵ_0 .

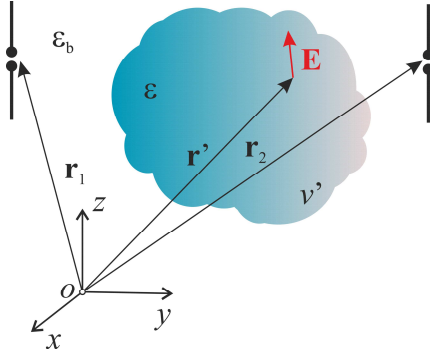


Fig. 1. Measurement scenario.

The measurements are taken by an array consisting of M antennas, out of which only two are shown in Fig. 1. The differential transmission coefficient between the i -th and the j -th antenna due to the presence of the object is given by [11]:

$$\Delta s_{ji} = -\frac{j\omega}{2a_i a_j} \int \Delta \epsilon(\mathbf{r}') \mathbf{E}^j(\mathbf{r}'; \epsilon_b) \cdot \mathbf{E}^i(\mathbf{r}'; \epsilon) dv', \quad (1a)$$

$$\Delta s_{ji} = s_{ji}(\epsilon) - s_{ji}(\epsilon_b), \quad i, j = 1, \dots, M, \quad (1b)$$

$$\Delta \epsilon(\mathbf{r}') = \epsilon(\mathbf{r}') - \epsilon_b(\mathbf{r}') \quad (1c)$$

where ω is the angular frequency, $s_{ji}(\epsilon)$ is the transmission coefficients computed (or measured) in the presence of the scatterer, $s_{ji}(\epsilon_b)$ is the transmission coefficient computed when the object is removed and substituted by the background medium, \mathbf{r}' is the position vector of a point inside the object, $\mathbf{E}^j(\mathbf{r}'; \epsilon_b)$ is the electric field vector produced by the j -th antenna at \mathbf{r}' in the background medium (the incident field), $\mathbf{E}^i(\mathbf{r}'; \epsilon)$ is the electric field vector produced by the i -th antenna at \mathbf{r}' when the object is present (the total field), a_i and a_j are the complex amplitudes of the incident power waves at the i -th and j -th port, respectively.

If the estimate of the target permittivity ($\hat{\epsilon}$) is utilized instead of the background permittivity (ϵ_b), (1) becomes

$$\Delta s_{ji} = -\frac{j\omega}{2a_i a_j} \int \Delta \epsilon(\mathbf{r}') \mathbf{E}^j(\mathbf{r}'; \hat{\epsilon}) \cdot \mathbf{E}^i(\mathbf{r}'; \epsilon) dv', \quad (2a)$$

$$\Delta s_{ji} = s_{ji}(\epsilon) - s_{ji}(\hat{\epsilon}), \quad i, j = 1, \dots, M, \quad (2b)$$

$$\Delta \epsilon(\mathbf{r}') = \epsilon(\mathbf{r}') - \hat{\epsilon}(\mathbf{r}'). \quad (2c)$$

Since the object permittivity is unknown, the Born approximation is utilized, $\mathbf{E}^i(\mathbf{r}'; \epsilon) \approx \mathbf{E}^i(\mathbf{r}'; \hat{\epsilon})$. Thus, (2a) becomes

$$\Delta s_{ji} \approx -\frac{j\omega}{2a_i a_j} \int \Delta \epsilon(\mathbf{r}') \mathbf{E}^j(\mathbf{r}'; \hat{\epsilon}) \cdot \mathbf{E}^i(\mathbf{r}'; \hat{\epsilon}) dv'. \quad (3)$$

In the limit when $\hat{\epsilon} \approx \epsilon$, the left-hand side of (3) approaches zero. The equation (3) is fundamental for DBIM.

In order to apply DBIM, it is necessary to divide the domain of interest into smaller domains (voxels), v_k , $k = 1, \dots, L$. We assume that all voxels have the same volume ΔV , which has to be sufficiently small so that the permittivity is approximately constant in each voxel. We use ϵ_k and $\hat{\epsilon}_k$ to denote the true and estimated complex permittivity of the k -th voxel.

DBIM is an iterative algorithm that needs to be initialized. If there is no prior knowledge about the permittivity of the inspected object, typically, the background permittivity is utilized, i.e., $\epsilon_k^{(1)} = \epsilon_{b,k}$, where $\epsilon_{b,k}$ is the permittivity of the background medium in the k -th voxel and the superscript (1) denotes the iteration number. In the i -th iteration, the linear system of equations is

$$\Delta \mathbf{s}^{(i)} = \mathbf{L}^{(i)} \Delta \boldsymbol{\epsilon}^{(i)}, \quad (4)$$

where $\Delta \mathbf{s}^{(i)}$ is a known vector whose elements are differences of the scattering parameters,

$$\Delta \mathbf{s}^{(i)} = [\Delta s_{1,1}^{(i)} \quad \Delta s_{1,2}^{(i)} \quad \dots \quad \Delta s_{M,M}^{(i)}]^T, \quad (5a)$$

$$\Delta s_{ij}^{(i)} = s_{ij}(\epsilon) - s_{ij}(\hat{\epsilon}^{(i)}), \quad i, j = 1, \dots, M, \quad (5b)$$

$\hat{\epsilon}^{(i)}$ is the current permittivity estimate

$$\hat{\epsilon}^{(i)} = [\hat{\epsilon}_1^{(i)} \quad \hat{\epsilon}_2^{(i)} \quad \dots \quad \hat{\epsilon}_L^{(i)}]^T, \quad (6)$$

$\mathbf{L}^{(i)}$ is the system matrix

$$\mathbf{L}^{(i)} = -\frac{j\omega \Delta V}{2} \begin{bmatrix} \frac{\mathbf{E}^1(\mathbf{q}_1; \hat{\epsilon}^{(i)}) \cdot \mathbf{E}^1(\mathbf{q}_1; \hat{\epsilon}^{(i)})}{a_1 a_1} & \dots & \frac{\mathbf{E}^1(\mathbf{q}_L; \hat{\epsilon}^{(i)}) \cdot \mathbf{E}^1(\mathbf{q}_L; \hat{\epsilon}^{(i)})}{a_1 a_1} \\ \frac{\mathbf{E}^1(\mathbf{q}_1; \hat{\epsilon}^{(i)}) \cdot \mathbf{E}^2(\mathbf{q}_1; \hat{\epsilon}^{(i)})}{a_1 a_2} & \dots & \frac{\mathbf{E}^1(\mathbf{q}_L; \hat{\epsilon}^{(i)}) \cdot \mathbf{E}^2(\mathbf{q}_L; \hat{\epsilon}^{(i)})}{a_1 a_2} \\ \vdots & \dots & \vdots \\ \frac{\mathbf{E}^M(\mathbf{q}_1; \hat{\epsilon}^{(i)}) \cdot \mathbf{E}^M(\mathbf{q}_1; \hat{\epsilon}^{(i)})}{a_M a_M} & \dots & \frac{\mathbf{E}^M(\mathbf{q}_L; \hat{\epsilon}^{(i)}) \cdot \mathbf{E}^M(\mathbf{q}_L; \hat{\epsilon}^{(i)})}{a_M a_M} \end{bmatrix}, \quad (7)$$

and $\Delta \boldsymbol{\epsilon}^{(i)}$ is an unknown vector

$$\Delta \boldsymbol{\epsilon}^{(i)} = [\Delta \epsilon_1^{(i)} \quad \Delta \epsilon_2^{(i)} \quad \dots \quad \Delta \epsilon_L^{(i)}]^T, \quad (8)$$

whose elements are the permittivity updates. The system (4) is solved by means of truncated singular value decomposition. The regularized solution is

$$\Delta \boldsymbol{\epsilon}^{(i)} = \sum_{n=1}^{n_{\max}} \frac{1}{\sigma_n} (\mathbf{u}_n^H \cdot \Delta \mathbf{s}^{(i)}) \mathbf{v}_n, \quad (9)$$

where \mathbf{u}_n , \mathbf{v}_n are the singular vectors of matrix $\mathbf{L}^{(i)}$, σ_n are the corresponding singular values, and n_{\max} is the truncation index, obtained from the condition $10 \log_{10} (\sigma_{n_{\max}} / \sigma_1) < -20$ dB. The permittivity estimate in the next iteration is obtained as

$$\hat{\boldsymbol{\epsilon}}^{(i+1)} = \hat{\boldsymbol{\epsilon}}^{(i)} + \Delta\hat{\boldsymbol{\epsilon}}^{(i)}, \quad (9)$$

The iterative algorithm terminates when the magnitude of each member of the vector $\Delta\boldsymbol{\epsilon}^{(i)}$ is smaller than some predefined value.

In some cases, prior knowledge about the tissue is available, i.e., from MRI scans. In these situations, we estimate the tissue permittivity, assuming that their surface boundaries are known. Thus, we can reduce the number of unknowns to the number of tissues. The measurement model becomes

$$\Delta\mathbf{s}^{(i)} = \mathbf{L}^{(i)}\mathbf{H}\Delta\boldsymbol{\epsilon}^{(i)}, \quad (10)$$

where \mathbf{H} is the transformational matrix of size $L \times N$, and N is the number of tissues. The (k,j) element of \mathbf{H} is one if v_k belongs to j -th domain and zero otherwise. The unknown vector is now

$$\Delta\boldsymbol{\epsilon}^{(i)} = [\Delta\epsilon_1^{(i)} \quad \Delta\epsilon_2^{(i)} \quad \dots \quad \Delta\epsilon_N^{(i)}]^T, \quad (11)$$

where $\Delta\epsilon_j^{(i)}$ refers to the j -th domain.

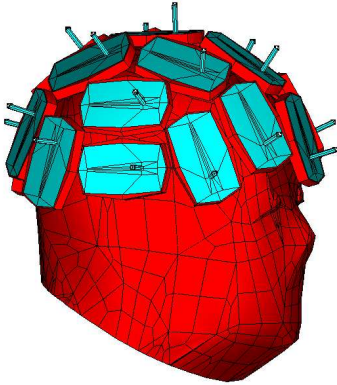


Fig. 2. Head model and the antenna array.

III. NUMERICAL RESULTS

In order to test the DBIM algorithm, we considered a realistic head model derived from the NEVA woman model [12]–[14]. The antenna array consisted of 21 identical microstrip trapezoidal patch antennas described in [12]. The antennas were fed by coaxial cables as illustrated in Fig. 2. The operating frequency of the array was 1 GHz, as this frequency is found to be the optimal in terms of both penetration depth and resolution.

The forward simulations were computed using the full-wave electromagnetic solver WIPL-D Pro [15]. All results presented in this paper are generated using a desktop computer: Intel Core i7-9700 CPU @3 GHz, NVIDIA GeForce GTX 750 Ti GPU, with 32 GB of RAM under the Windows 10 operating system.

In the first example, the goal was to find the equivalent homogeneous head phantom, which is equivalent (in terms of scattering parameters) to the realistic head phantom comprising seven tissues (skin, fat, mucous membrane, skull, gray matter, white matter and cerebellum).

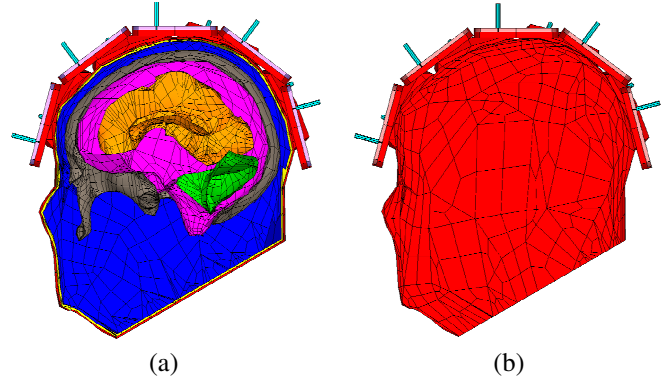


Fig. 3. (a) Reference head model with seven tissues. (b) Equivalent homogeneous head model filled with the average tissue.

The head interior was divided into $L = 8676$ voxels. As there was only one domain (averaged tissue), the transformation matrix \mathbf{H} was a column vector of size $L \times 1$ with all elements being equal to one. As the initial permittivity estimate, we used the value calculated by the standard averaging procedure $\epsilon_r^{(1)} = 41.47 - j14.15$ [12]. After six iterations, the permittivity value converged to $\epsilon_r^{(6)} = 34.64 - j12.68$. As a comparison, the gradient optimization [12] yielded for the average tissue permittivity $\epsilon_r = 34.68 - j12.68$, which is almost the same result. The number of unknowns in the WIPL-D model (current coefficients) for this example was 24109, and an iteration lasted about 6 minutes.

In the second scenario, the goal was to reconstruct the permittivities of five tissues (skin, fat, mucous membrane, skull, and gray matter) from the head model shown in Fig. 4, assuming that the tissue boundaries are known. As the initial permittivity, we used the value obtained in the first experiment, $\epsilon_r^{(1)} = 34.64 - j12.68$, for all tissues.

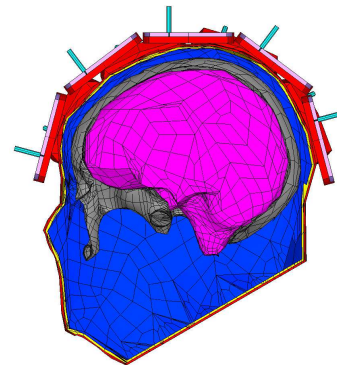


Fig. 4. Model with five tissues.

The WIPL-D model with five tissues has 48354 unknowns and each iteration lasted about 55 minutes. The results obtained after 20 iterations of the algorithm are shown in Table I. The true permittivities of tissues are given in the second column, and the estimated permittivities are shown in the third column. The last column indicates the number of voxels per each tissue.

TABLE I. ESTIMATION RESULTS FOR THE HEAD WITH FIVE TISSUES

Tissue Name	ϵ_r	$\epsilon_r^{(20)}$	Number of voxels
Skin	45.71 – j15.84	45.79 – j15.82	3445
Fat	11.29 – j2.09	11.27 – j2.17	5086
Mucous Membrane	45.66 – j15.95	45.64 – j15.94	35340
Grey Matter	52.28 – j17.71	52.28 – j17.71	18267
Skull Bone	20.58 – j6.54	20.59 – j6.55	7179

In the last example, the goal was to reconstruct the permittivities of the head phantom with seven tissues (Fig. 3a), assuming that the tissue boundaries are known. Again, all elements of the vector $\epsilon^{(1)}$ were initialized with the averaged tissue value $\epsilon_r = 34.64 - j12.68$. Firstly, we ran the algorithm with a smaller number of voxels for 20 iterations, and each of them lasted about 60 minutes. We used the obtained results as the initial guess for the permittivities for the next 10 iterations with an increased number of voxels. The execution time of each of those iterations was about 105 minutes. The number of unknowns in the WIPL-D model for this scenario was 60778. Table II shows the results obtained after all 30 iterations.

TABLE II. ESTIMATION RESULTS FOR THE HEAD WITH SEVEN TISSUES

Tissue Name	ϵ_r	$\epsilon_r^{(30)}$	Number of voxels
Skin	45.71 – j15.84	45.69 – j15.85	463/3445
Fat	11.29 – j2.09	11.33 – j2.03	655/5086
Mucous Membrane	45.66 – j15.95	45.73 – j15.92	4480/35340
Grey Matter	52.28 – j17.71	52.42 – j17.91	1690/13285
Skull Bone	20.58 – j6.54	20.67 – j6.70	903/7179
White Matter	38.58 – j11.18	38.33 – j11.27	492/3864
Cerebellum	48.86 – j23.51	34.66 – j12.65	140/1118

The biggest error was obtained for the cerebellum permittivity, which is the smallest domain located deep inside the head. The estimated permittivity values are shown in Fig. 5 (dots at the end represent the true values). Moreover, it can be observed that the cerebellum permittivity has changed insignificantly. Thus, we ran additional 10 iterations of DBIM for estimating the permittivity of the cerebellum, while the permittivities of other six tissues were fixed to the values obtained after 30 iterations. Finally, the permittivity of the cerebellum converged closely to the true value ($\epsilon_r^{(40)} = 48.80 - j23.51$).

IV. CONCLUSION

We studied the capability of the DBIM to estimate the permittivities of tissues in realistic human head phantoms. We considered phantoms of different complexity and utilized the simplest model to initialize more elaborate ones. The permittivity was accurately estimated under the assumption that tissue boundaries are known. We will consider the case in which no prior knowledge is available in future work. However, voxel-based meshing has to be utilized in that case, which yields a significantly larger number of unknowns in the forward electromagnetic model and, consequently, increases the computational time enormously.

ACKNOWLEDGMENT

This work was supported by the EMERALD project funded from the European Union's Horizon 2020 research and innovation program under the Marie Skłodowska-Curie grant agreement No. 764479.

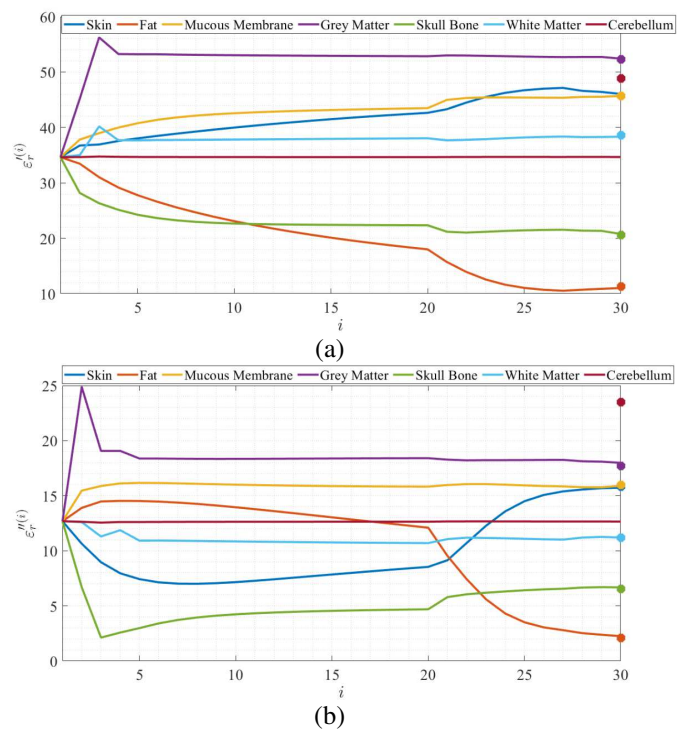


Fig. 5. Estimated permittivities of tissues for each iteration. (a) Real and (b) imaginary part of the complex permittivity.

REFERENCES

- [1] R. Chandra, H. Zhou, I. Balasingham and R. M. Narayanan, "On the Opportunities and Challenges in Microwave Medical Sensing and Imaging," *IEEE Transactions on Biomedical Engineering*, vol. 62, no. 7, pp. 1667-1682, July 2015.
- [2] L. Crocco, I. Karanasiou, M. James, R. Conceição, "Emerging Electromagnetic Technologies for Brain Diseases Diagnostics, Monitoring and Therapy," *Springer*, Cham, Switzerland, 2018.
- [3] R. Conceição, J. Mohr, M. O'Halloran, "An Introduction to Microwave Imaging for Breast Cancer Detection," Switzerland, Springer, 2018.
- [4] G. Zhu, A. Bialkowski, L. Guo, B. Mohammed and A. Abbosh, "Stroke Classification in Simulated Electromagnetic Imaging Using Graph Approaches," *IEEE Journal of Electromagnetics, RF and Microwaves in Medicine and Biology*, vol. 5, no. 1, pp. 46-53, March 2021.
- [5] A. S. M. Alqadami, A. Trakic, A. E. Stancombe, B. Mohammed, K. Bialkowski and A. Abbosh, "Flexible Electromagnetic Cap for Head

- Imaging," *IEEE Transactions on Biomedical Circuits and Systems*, vol. 14, no. 5, pp. 1097-1107, Oct. 2020.
- [6] J. D. Shea, B. D. Van Veen and S. C. Hagness, "A TSVD Analysis of Microwave Inverse Scattering for Breast Imaging," *IEEE Transactions on Biomedical Engineering*, vol. 59, no. 4, pp. 936-945, April 2012.
- [7] L. Crocco, I. Catapano, L. Di Donato and T. Isernia, "The Linear Sampling Method as a Way to Quantitative Inverse Scattering," *IEEE Transactions on Antennas and Propagation*, vol. 60, no. 4, pp. 1844-1853, April 2012.
- [8] G. Bozza, C. Estatico, M. Pastorino, and A. Randazzo, "An Inexact Newton Method for Microwave Reconstruction of Strong Scatterers," in *IEEE Antennas and Wireless Propagation Letters*, vol. 5, pp. 61-64, 2006.
- [9] L. Guo, N. Nguyen-Trong, A. Al-Saffar, A. Stacombe, K. Bialkowski and A. Abbosh, "Calibrated Frequency-Division Distorted Born Iterative Tomography for Real-Life Head Imaging," in *IEEE Transactions on Medical Imaging*, doi: 10.1109/TMI.2021.3132000.
- [10] L. Guo, M. Khosravi-Farsani, A. Stacombe, K. Bialkowski and A. Abbosh, "Adaptive Clustering Distorted Born Iterative Method for Microwave Brain Tomography With Stroke Detection and Classification," in *IEEE Transactions on Biomedical Engineering*, vol. 69, no. 4, pp. 1512-1523, April 2022.
- [11] Nikolova, N. Introduction to Microwave Imaging, *EuMA High Frequency Technologies Series*, Cambridge University Press, Cambridge.
- [12] T. Singh et al., "New Method for Calculation of Average Electric Properties of Reference Head Phantom in Microwave Imaging," 2022 16th European Conference on Antennas and Propagation (EuCAP), 2022, pp. 1-5.
- [13] S. N. Makarov, G. M. Noetscher, J. Yanamadala, M. W. Piazza, AU - S. Louie, A. Prokop, A. Nazarian, A. Nummenmaa "Virtual Human Models for Electromagnetic Studies and Their Applications," in *IEEE Reviews in Biomedical Engineering*, vol. 10, pp. 95-121, 2017, doi: 10.1109/RBME.2017.2722420.
- [14] <https://www.nevaelectromagnetics.com/>
- [15] WIPL-D Pro v17 [Online]. Available: <http://www.wipl-d.com/>.

Current distribution in a hollow cylindrical conductor influenced by a parallel filament

Dragan Filipović, Tatijana Dlabáč

Abstract—This paper presents a rigorous solution for the current distribution in a hollow cylindrical conductor in the presence of a current filament placed outside the conductor. The currents are assumed low-frequency, time-harmonic, flowing in opposite directions. As a starting point, we chose a Fredholm-type integral equation for the current density whose solution is sought in the form of an infinite sum of the proper harmonics – the modified Bessel functions of the second kind and trigonometric functions. The unknown coefficients in the sum are determined by equating the coefficients standing with the corresponding functions on both sides of the integral equation. The method presented in the paper allows treatment of the cases when the filament is inside the conductor and /or the currents have the same direction.

Index Terms—current distribution; hollow conductor; filament; integral equation

I. INTRODUCTION

Determination of current distribution in a system of parallel cylindrical conductors with time-varying currents is a very complex problem since this distribution in each of the conductors is not only affected by its own electromagnetic field (skin effect), but also by the fields of all other conductors (proximity effect). There are very few cases where this problem can be solved in a closed form, so generally an implementation of various numerical methods is required. Among the most commonly used approaches to the combined skin and proximity effects we mention here: usage of Maxwell's equations in terms of the magnetic vector potential [1–4], method of integral equations [5–11], boundary integral equation formulation [12,13], method of model functions [14], etc.

In this paper we use an integral equation to solve in a closed form the problem of low-frequency current distribution in a cylindrical hollow conductor in the presence of an outer current filament, the currents being assumed sinusoidal and to flow in opposite directions. The solution is sought in the form of an infinite sum of proper harmonics with some unknown coefficients. These coefficients are found in a closed form by equating coefficients with the corresponding functions on both sides of the integral equation.

Dragan Filipović is with the Faculty of Electrical Engineering, University of Montenegro, 81000 Podgorica, Montenegro (e-mail: draganf@ucg.ac.me), (<https://orcid.org/0000-0001-8652-0661>)

Tatijana Dlabáč is with the Maritime Faculty Kotor, University of Montenegro, 85330 Kotor, Montenegro (e-mail: tanjav@ucg.ac.me), (<https://orcid.org/0000-0001-9473-5558>)

II. INTEGRAL EQUATION FOR THE CURRENT DENSITY IN A HOLLOW CYLINDRICAL CONDUCTOR IN THE PRESENCE OF A FILAMENT

Geometry of the problem is shown in Fig. 1. A current filament is parallel to a massive hollow cylindrical conductor of radii a and b .

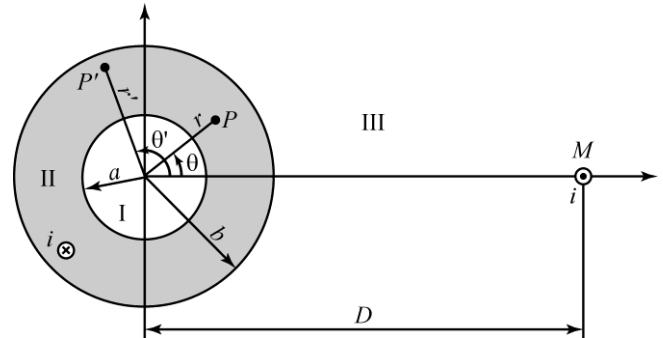


Fig. 1. Massive hollow cylindrical conductor and filament

The distance between the filament and the conductor axis is D , and the parameters of the conductor are σ and μ_0 . Currents of equal r.m.s. I and of frequency f flow through the conductor and the filament in opposite directions. The objective is to find the current distribution in the massive conductor.

Following [5]-[6], [9], [11], we can write an integral equation for current density in the conductor:

$$J(r, \theta) = \frac{k^2}{4\pi} \left[\int_S r' J(r', \theta') \ln \frac{r^2 + r'^2 - 2rr' \cos(\theta - \theta')}{D^2} dr' d\theta' - I \ln \frac{r^2 + D^2 - 2rD \cos \theta}{D^2} \right] + K, \quad (1)$$

where $k^2 = j\omega\mu_0\sigma$, K is an unknown constant, and S is the annulus $a \leq r \leq b$, $0 \leq \theta \leq 2\pi$.

Current density $J(r, \theta)$ in (1) is subject to the condition:

$$\int_S J(r, \theta) r dr d\theta = I. \quad (2)$$

III. SOLUTION OF THE INTEGRAL EQUATION

Separation of variables in the wave equation for current density leads to the following particular solutions (harmonics): $I_n(kr)$, $K_n(kr)$, $\cos n\theta$, $\sin n\theta$, where I_n and K_n are

modified Bessel functions. Symmetry requires that $J(r, \theta)$ be an even function in θ , which eliminates $\sin n\theta$. Hence, an appropriate form of the solution of (1) is

$$J(r, \theta) = \sum_{n=0}^{\infty} [A_n I_n(kr) + B_n K_n(kr)] \cos n\theta \quad (3)$$

with some unknown coefficients A_n and B_n . When (3) is substituted into (1), we obtain

$$\begin{aligned} & \sum_{n=0}^{\infty} [A_n I_n(kr) + B_n K_n(kr)] \cos n\theta = \\ & = \frac{k^2}{4\pi} \sum_{n=0}^{\infty} A_n F_n(r, \theta) + \frac{k^2}{4\pi} \sum_{n=0}^{\infty} B_n G_n(r, \theta) + \\ & + \frac{k^2 I}{2\pi} \sum_{n=1}^{\infty} \left(\frac{r}{D}\right)^n \frac{\cos n\theta}{n} + K \end{aligned} \quad (4)$$

where

$$F_n(r, \theta) = \begin{cases} \frac{4\pi}{k} \left[b \ln \frac{b}{D} I_1(kb) - a \ln \frac{r}{D} I_1(ka) \right] - \frac{4\pi}{k^2} [I_0(kb) - I_0(kr)], & n = 0 \\ \left\{ -\frac{2\pi}{nk} \left[b \left(\frac{r}{b}\right)^n I_{n-1}(kb) - a \left(\frac{a}{r}\right)^n I_{n+1}(ka) \right] + \frac{4\pi}{k^2} I_n(kr) \right\} \cos n\theta, & n > 0 \end{cases} \quad (8)$$

$$G_n(r, \theta) = \begin{cases} \frac{4\pi}{k} \left[a \ln \frac{r}{D} K_1(ka) - b \ln \frac{b}{D} K_1(kb) \right] - \frac{4\pi}{k^2} [K_0(kb) - K_0(kr)], & n = 0 \\ \left\{ -\frac{2\pi}{nk} \left[a \left(\frac{a}{r}\right)^n K_{n-1}(ka) - b \left(\frac{r}{b}\right)^n K_{n-1}(kb) \right] + \frac{4\pi}{k^2} K_n(kr) \right\} \cos n\theta, & n > 0 \end{cases} \quad (9)$$

With F_n and G_n given by (8) - (9), we can equate the constant terms and the coefficients with $\ln(r/D)$, $r^n \cos n\theta$ and $r^{-n} \cos n\theta$ on both sides of (4), to get respectively

$$\begin{aligned} 0 &= A_0 \left(kb \ln \frac{b}{D} I_1(kb) - I_0(kb) \right) + \\ &+ B_0 \left(-kb \ln \frac{b}{D} K_1(kb) - K_0(kb) \right) + K \end{aligned} \quad (10)$$

$$0 = -A_0 I_1(ka) + B_0 K_1(ka) \quad (11)$$

$$0 = -A_n I_{n-1}(kb) + B_n K_{n-1}(kb) + \frac{kI}{\pi b} \left(\frac{b}{D}\right)^n \quad (12)$$

$$0 = A_n I_{n+1}(ka) - B_n K_{n+1}(ka). \quad (13)$$

To determine the five unknown constants (A_0, B_0, A_n, B_n and K) we need one more equation beside the four equations given by (10) - (13). This additional equation is obtained from (2) if we replace $J(r, \theta)$ by (3). Then, we have

$$F_n(r, \theta) = \int_S r' I_n(kr') \ln \frac{r^2 + r'^2 - 2rr' \cos(\theta - \theta')}{D^2} dr' d\theta' \quad (5)$$

$$G_n(r, \theta) = \int_S r' K_n(kr') \ln \frac{r^2 + r'^2 - 2rr' \cos(\theta - \theta')}{D^2} dr' d\theta' \quad (6)$$

and we made use of [15]

$$\ln \left(1 + \frac{r^2}{D^2} - \frac{2r}{D} \cos \theta \right) = -2 \sum_{n=1}^{\infty} \left(\frac{r}{D}\right)^n \frac{\cos n\theta}{n}, \quad \frac{r}{D} < 1. \quad (7)$$

The double integrals F_n and G_n , given by (5) - (6), seemingly very complex, can be evaluated in a closed form. This is done in the Appendix for F_n ; G_n is found in the same way. Here we state the result.

$$\begin{aligned} I &= \int_0^{2\pi} d\theta \int_a^b r J(r, \theta) dr = \\ &= \sum_{n=0}^{\infty} \int_0^{2\pi} \cos n\theta \int_a^b r (A_n I_n(kr) + B_n K_n(kr)) dr = \\ &= A_0 2\pi \int_a^b r I_0(kr) dr + B_0 2\pi \int_a^b r K_0(kr) dr. \end{aligned} \quad (14)$$

The integrals in (14) are readily evaluated by making the change of variables $kr = x$ and using the identities [16]

$$xI_0(x) = (xI_1(x))'$$

$$xK_0(x) = -(xK_1(x))'$$

Hence (14) becomes

$$I = \frac{2\pi}{k} \{ A_0 [bI_1(kb) - aI_1(ka)] + B_0 [aK_1(ka) - bK_1(kb)] \}. \quad (15)$$

Now, (11) and (15) can be solved for A_0 and B_0

$$A_0 = \frac{kI}{2\pi b} \frac{K_1(ka)}{I_1(kb)K_1(ka) - I_1(ka)K_1(kb)} \quad (16)$$

$$B_0 = \frac{kI}{2\pi b} \frac{I_1(ka)}{I_1(kb)K_1(ka) - I_1(ka)K_1(kb)} \quad (17)$$

and A_n, B_n are found from (12) - (13)

$$A_n = \frac{kI}{\pi b} \left(\frac{b}{D}\right)^n \frac{K_{n+1}(ka)}{K_{n+1}(ka)I_{n-1}(kb) - K_{n-1}(kb)I_{n+1}(ka)} \quad (18)$$

$$B_n = \frac{kI}{\pi b} \left(\frac{b}{D}\right)^n \frac{I_{n+1}(ka)}{K_{n+1}(ka)I_{n-1}(kb) - K_{n-1}(kb)I_{n+1}(ka)}. \quad (19)$$

The remaining unknown K can be determined from (10), (16) - (17), but it is of no importance.

Finally, (3) and (16) - (19) determine current density in the massive conductor

$$J(r, \theta) = \frac{kI}{2\pi b} \frac{K_1(ka)I_0(kr) + I_1(ka)K_0(kr)}{I_1(kb)K_1(ka) - I_1(ka)K_1(kb)} + \frac{kI}{\pi b} \sum_{n=1}^{\infty} \left(\frac{b}{D}\right)^n \frac{K_{n+1}(ka)I_n(kr) + I_{n+1}(ka)K_n(kr)}{I_{n-1}(kb)K_{n+1}(ka) - I_{n+1}(ka)K_{n-1}(kb)} \cos n\theta. \quad (20)$$

Physically, the first term on the right-hand side of (20) is due to the skin effect, and the infinite sum accounts for the influence of the filament (proximity effect).

$$\begin{aligned} F_0(r, \theta) &= \int_0^{2\pi} a\theta' \int_a^b r'I_0(kr') \ln \frac{r^2 + r'^2 - 2rr' \cos(\theta - \theta')}{D^2} dr' = \\ &= \int_0^{2\pi} a\theta' \left[\int_a^r r'I_0(kr') \ln r^2 \frac{r^2 + r'^2 - 2rr' \cos(\theta - \theta')}{r^2 D^2} dr' + \int_r^b r'I_0(kr') \ln r'^2 \frac{r^2 + r'^2 - 2rr' \cos(\theta - \theta')}{r'^2 D^2} dr' \right] = \\ &= \int_0^{2\pi} a\theta' \left\{ \int_a^r r'I_0(kr') \left[\ln \frac{r^2}{D^2} + \ln \left(1 + \frac{r'^2}{r^2} - 2 \frac{r'}{r} \cos(\theta - \theta') \right) \right] dr' + \int_r^b r'I_0(kr') \left[\ln \frac{r'^2}{D^2} + \ln \left(1 + \frac{r^2}{r'^2} - 2 \frac{r'}{r} \cos(\theta - \theta') \right) \right] dr' \right\} \\ &= \int_0^{2\pi} a\theta' \left[\ln \frac{r^2}{D^2} \int_a^r r'I_0(kr') dr - 2 \int_a^r r'I_0(kr') \sum_{m=1}^{\infty} \left(\frac{r'}{r}\right)^m \frac{\cos m(\theta - \theta')}{m} dr' + \int_r^b r' \ln \frac{r'^2}{D^2} I_0(kr') dr - 2 \int_r^b r'I_0(kr') \sum_{m=1}^{\infty} \left(\frac{r}{r'}\right)^m \frac{\cos m(\theta - \theta')}{m} dr' \right] \end{aligned} \quad (A1)$$

where we used (7). We do not need to evaluate the integrals that include infinite sum, since $\cos m(\theta - \theta') = \cos m\theta \cos m\theta' + \sin m\theta \sin m\theta'$, and the subsequent integration in θ' gives zero, since $\int_0^{2\pi} \cos m\theta' d\theta' = \int_0^{2\pi} \sin m\theta' d\theta' = 0, m \geq 1$. The two remaining integrals are evaluated as follows

The same method applies if the filament is inside the conductor. In this case b/D in the infinite sum in (20) should be replaced by D/b .

Expression (20) may also be derived by using Maxwell's equations [4]. In this approach the magnetic vector potential is determined in media I, II and III (Fig. 1), which includes usage of appropriate boundary conditions on the interfaces $r=a$ and $r=b$. The approach in the present paper is much simpler – solving integral equation (1) does not involve any boundary conditions.

It may be shown that the particular cases $a=0$ (massive conductor [6], [11]), and $b-a=d \ll a$ (thin tubular conductor [5], [9]), follow from (20). Derivation for the former case is straightforward; for the latter case, it requires usage of a few formulas that involve Bessel functions.

IV. CONCLUSION

In this paper, we derived a closed-form solution for the current distribution in a hollow cylindrical conductor in the presence of a current filament placed outside the conductor. A solution of an integral equation for the current density is found in the form of an infinite sum of proper harmonics - the modified Bessel functions of the second kind and the trigonometric functions. A remarkable feature of the method used is that it does not involve any boundary conditions.

APPENDIX

In this Appendix we prove (8), relation (9) is justified by the same procedure.

Let $n=0$. Then

$$\int_a^r r'I_0(kr') dr' = \frac{1}{k^2} \int_{ka}^{kr} u I_0(u) du = \frac{1}{k} (r I_1(kr) - a I_1(ka)), \quad (A2)$$

where the change of variables $kr'=u$ and the identity

$$u I_0(u) = (u I_1(u))',$$

were used. Similarly, by using integration by parts

$$\int_r^b r' \ln \frac{r'^2}{D^2} I_0(kr') dr' = \frac{2}{k^2} \int_{kr}^{kb} u \ln \frac{u}{kD} I_0(u) du =$$

$$= \frac{2}{k^2} \left[u I_1(u) \ln \frac{u}{kD} \Big|_{kr}^{kb} - \int_{kr}^{kb} u I_1(u) \frac{du}{u} \right] =$$

$$= \frac{2}{k^2} \left(kb \ln \frac{b}{D} I_1(kb) - kr \ln \frac{r}{D} I_1(kr) - \int_{kr}^{kb} I_1(u) du \right) =$$

$$= \frac{2}{k^2} \left[kb \ln \frac{b}{D} I_1(kb) - kr \ln \frac{r}{D} I_1(kr) - (I_0(kb) - I_0(kr)) \right]$$

since [16]

$$I_1(u) = I_0'(u).$$

Now, relation (8) for $n = 0$ follows from (A1) - (A3).

For $n \geq 1$

$$F_n(r, \theta) = \int_0^{2\pi} \cos n\theta' d\theta' \left[\ln \frac{r'^2}{D^2} \int_a^r r' I_n(kr') dr' - \right.$$

$$- 2 \int_a^r r' I_n(kr') \sum_{m=1}^{\infty} \left(\frac{r'}{r} \right)^m \frac{\cos m(\theta - \theta')}{m} dr' +$$

$$\left. + \int_r^b r' \ln \frac{r'^2}{D^2} I_n(kr') dr' - 2 \int_r^b r' I_n(kr') \sum_{m=1}^{\infty} \left(\frac{r'}{r} \right)^m \frac{\cos m(\theta - \theta')}{m} dr' \right] d\theta'$$

In this case, the integrals $\int_a^r r' I_n(kr') dr'$ and

$\int_r^b r' \ln \frac{r'^2}{D^2} I_n(kr') dr'$ are irrelevant, since the subsequent

integration in θ' gives zero $\left(\int_0^{2\pi} \cos n\theta' d\theta' = 0, n \geq 1 \right)$, hence

(A4) becomes

$$F_n(r, \theta) = -2 \sum_{m=1}^{\infty} \frac{1}{m r^m} \int_0^{2\pi} \cos n\theta' \cos m(\theta - \theta') d\theta' \int_a^r r'^{m+1} I_m(kr') dr' -$$

$$- 2 \sum_{m=1}^{\infty} \frac{r^m}{m} \int_0^{2\pi} \cos n\theta' \cos m(\theta - \theta') d\theta' \int_r^b r'^{-m+1} I_m(kr') dr'.$$

Only the term with $m = n$ should be kept in the infinite sums, since for $m \neq n$

$$\int_0^{2\pi} \cos n\theta' \cos m(\theta - \theta') d\theta' =$$

$$= \cos n\theta \int_0^{2\pi} \cos n\theta' \cos m\theta' d\theta' + \sin m\theta \int_0^{2\pi} \cos n\theta' \sin m\theta' d\theta' = 0,$$

due to orthogonality of the sine and cosine functions. As a consequence, (A5) simplifies to

$$F_n(r, \theta) = \left(- \frac{2\pi}{nr^n} \int_a^r r'^{n+1} I_n(kr') dr' - \right.$$

$$\left. - \frac{2\pi r^n}{n} \int_r^b r'^{-n+1} I_n(kr') dr' \right) \cos n\theta$$

where we have taken into account that

$$\int_0^{2\pi} \cos n\theta' \cos n(\theta - \theta') d\theta' =$$

$$= \cos n\theta \int_0^{2\pi} \cos^2 n\theta' d\theta' + \sin n\theta \int_0^{2\pi} \cos n\theta' \sin n\theta' d\theta' = \pi \cos n\theta.$$

The change of variables $kr' = u$ and the relations [16]

$$u^{n+1} I_n(u) = (u^{n+1} I_{n+1}(u))'$$

$$u^{-n+1} I_n(u) = (u^{-n+1} I_{n-1}(u))'$$

enable to evaluate the two integrals in (A6)

$$\int_a^r r'^{n+1} I_n(kr') dr' = \frac{1}{k} (r^{n+1} I_{n+1}(kr) - a^{n+1} I_{n+1}(ka))$$

$$\int_r^b r'^{-n+1} I_n(kr') dr' = \frac{1}{k} (b^{-n+1} I_{n-1}(kb) - r^{-n+1} I_{n-1}(kr)).$$

Finally, from (A6) - (A8)

$$F_n(r, \theta) = - \frac{2\pi}{nk} \left\{ r [I_{n+1}(kr) - I_{n-1}(kr)] + b \left(\frac{r}{b} \right)^n I_{n+1}(kb) - \right.$$

$$\left. - a \left(\frac{a}{r} \right)^n I_{n+1}(ka) \right\} \cos n\theta =$$

$$= \left\{ - \frac{2\pi}{nk} \left[b \left(\frac{r}{b} \right)^n I_{n-1}(kb) - a \left(\frac{a}{r} \right)^n I_{n+1}(ka) \right] + \frac{4\pi}{k^2} I_n(kr) \right\} \cos n\theta$$

since [16]

$$I_{n+1}(kr) - I_{n-1}(kr) = - \frac{2n}{kr} I_n(kr).$$

Therefore, the proof of (8) is completed.

REFERENCES

- [1] P. Rolicz: "Skin effect in a system of two rectangular conductors carrying identical currents", Electrical Engineering 82 (2000) 285-290 © Springer-Verlag 2000

- [2] P. Dokopoulos, D. Tampakis, "Eddy current in system of tubular conductors", IEEE Trans. on magnetics, vol. MAG-20, no. 5, pp 1971 - 1973, 1984.
- [3] J. A. Tegopoulos, E. E. Kriezis, "Eddy current distribution in cylindrical shells of infinite length due to axial currents, Part I: Shells of one boundary", IEEE Trans. on Power Apparatus and Systems, vol. PAS-90, Issue:3 pp 1278 - 1286, 1971.
- [4] J. A. Tegopoulos, E. E. Kriezis, "Eddy current distribution in cylindrical shells of infinite length due to axial currents, Part II: Shells of finite thickness", IEEE Trans. on Power Apparatus and Systems, vol. PAS-90, Issue:3 pp 1287 - 1294, 1971.
- [5] H. B. Dwight, Electrical Coils and Conductors, Mc Graw-Hill, New York, 1945.
- [6] C. Manneback, "An integral equation for skin effect in parallel conductors", J. Math. Phys., vol. 1, pp. 123-146, Apr. 1922.
- [7] B. D. Popović, Z. D. Popović: "Method of determining power-frequency current distribution in cylindrical conductors", Proc. IEE, Vol. 119, no 5. May 1972, pp. 569-574.
- [8] B. Popović, D. Filipović, "Theory of power-frequency proximity effect for strip conductors", Proc. IEE, Vol. 122, no 8. August 1975, pp. 820-823.
- [9] D. Filipović, T. Dlabac, "A closed form solution for the proximity effect in a thin tubular conductor influenced by a parallel filament", Serbian Journal of Electr. Eng., vol. 7, no. 1, May 2010, 13-20
- [10] Dlabac T., Filipović D., Plazinić M., "Integral Equation Method for Determining Current Distribution in a System of Parallel Conductors", Technics Technologies Education Management (ISSN:1840-1503), vol. 7, no. 4, 11/12, 2012.
- [11] D. Filipović, T. Dlabac, "A closed form solution for the current density in a solid round conductor influenced by a filament", Proc. of the 54th ETRAN conference, Donji Milanovac, Serbia, 7 - 10 June 2010, (in Serbian).
- [12] M. Cao, P.P. Biringer, "BIE formulation for skin and proximity effect problems of parallel conductors", IEEE Trans. on magnetics, vol. 26, no. 5, September 1990, pp 2768 - 2770.
- [13] M. Cao, P.P. Biringer, "Asymmetry in bus bars due to proximity effects", J. Appl. Phys., vol. 67, no. 9, May 1990, pp. 4729-4731
- [14] P. Silvester, "Skin effect in multiple and polyphase conductors", IEEE Trans. on Power Apparatus and Systems, vol. PAS-88, no. 3, pp. 231-238, March 1969.
- [15] I. Gradshteyn and I. Ryzhik, Table of Integrals, Series, and Products, 7th ed. New York, NY, USA: Academic, 2007.
- [16] H. Bateman, A. Erdelyi, Higher Transcendental Functions, vol. 2, Mc Graw-Hill, New York, 1953.

Jamming a Drone - EM Simulation of Simple EW and EW Countermeasures Scenarios

Tomislav Milošević

Abstract—The paper discusses electromagnetic simulations (EM) of an electronic warfare (EW) scenario where a drone is jammed using a continuous wave (CW) jammer. EW countermeasures have been proposed based on calculated currents induced on specific parts of the drone critical for jamming effectiveness, such is antenna or wire in printed circuit board. All the simulations relate to widely used 2.4 GHz frequency band.

Index Terms—jamming, drone, anti-drone.

I. INTRODUCTION

VARIOUS types of drones exist on a consumer market spanning from pieces dedicated to sport or entertainment to high class devices capable to carry out complex tasks. Besides utilization of drones along with positive legislation, even drones with basic functionality can potentially be used for malicious activities in scenarios which are not socially tolerable or could even be harmful. For example, a very basic drone can be used by paparazzi in invading celebrities' privacy or by criminals and terrorists in compromising security of a potential target. Therefore, in parallel with development of the drones, various anti-drone systems have been developed as well.

This paper presents a scenario where a radio-controlled drone is flying within an active zone of an anti-drone system. Anti-drone system itself is simply a helix antenna with a reflector.

Communication systems in general may exhibit restricted or completely inhibited functionality when subjected to interference, jamming or outer EW measures [1], [2]. Described model of jamming system represents the class of anti-drone systems which uses a CW signal to jam the drone flight-control receiver. In order to reduce the effect of the jammer, simple passive countermeasures can be used. In general, passive countermeasures do not involve the emission of any signals or noise [1]. It will be shown that using the results of EM reconnaissance, a simple, partial shielding of the jamming sensitive parts of the drone can significantly reduce the effectiveness of the jamming. It is assumed that anti-drone system and the drone receiver both operate at 2.4 GHz, the frequency widely used for Wireless LAN [3].

The basic principle of an anti-drone system operation is to induce current – a strong jamming signal on the drone side and saturate the receiver. Also, it is possible that the anti-drone system induces current in the printed circuit board (PCB) which is a part of the drone electronic system causing

the malfunctioning of onboard electronics. Addressing the practical side of anti-drone system as described, one can say that receiving of control signals through the drone receiver will be blocked and that additionally a spurious signal would be induced in the electronic circuits.

The effects of the jamming will be simulated using WIPL-D Pro, a full wave 3D electromagnetic Method-of-Moments (MoM) based software which applies Higher Order Basis Functions over bilinear surfaces combined with Surface Integral Equations [4]. The software considers the bilinear surfaces as nonplanar quadrilaterals defined uniquely by four vertices [5]. Thanks to the inherent property of MoM, the size of EM model and accordingly the complexity of the simulation does not increase with increased jammer-to-drone distance [4].

II. MODEL OF THE DRONE

The model of the drone is shown in the Fig. 1. It contains a camera mounted below the drone, which represents a payload of the drone. The drone with its payload is modeled as a dielectric object with the following dielectric properties: $\epsilon_{r\text{Real}}=2.2$ and $\epsilon_{r\text{Imag}}=-0.066$. Beside the dielectric, the drone contains some metallic parts which are also shown in the Fig. 1. The “upper” metallic parts represent the monopole antenna with the ground plane. The monopole antenna is intended to be used for receiving flight control signals. The “lower” metallic parts represent a simplified PCB with a rectangular half-loop on it.

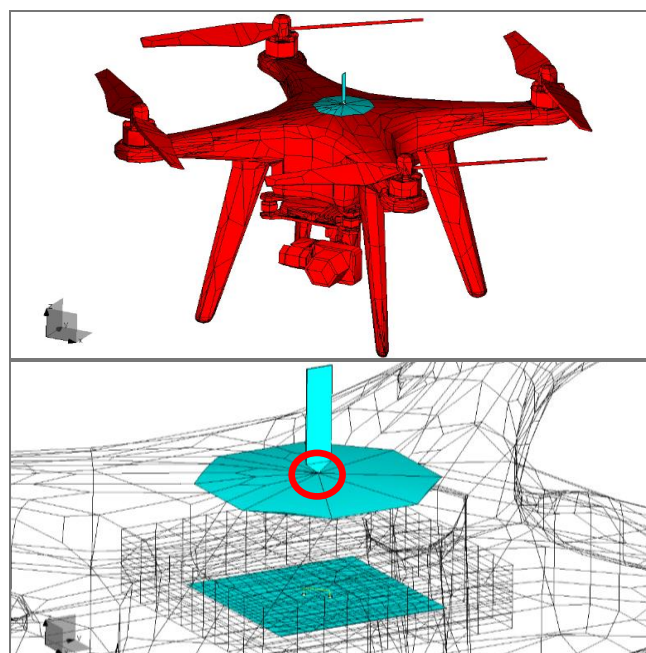


Figure 1. The model of the drone with the payload and the metallic parts of the drone.

Inducing the jamming current on the receiver will be monitored on the wire used to feed the monopole antenna. The wire is located at the very end of the antenna and it is encircled in red in Fig. 1.

The current induced in drone PCB is monitored on the grounded half-loop. Actually, as presented with markings outlined in the Fig. 2, the induced current is calculated over the “horizontal” wire. The dimensions of the metallic surface representing demonstration model of the PCB and the half-loop are also displayed in the Fig. 2.

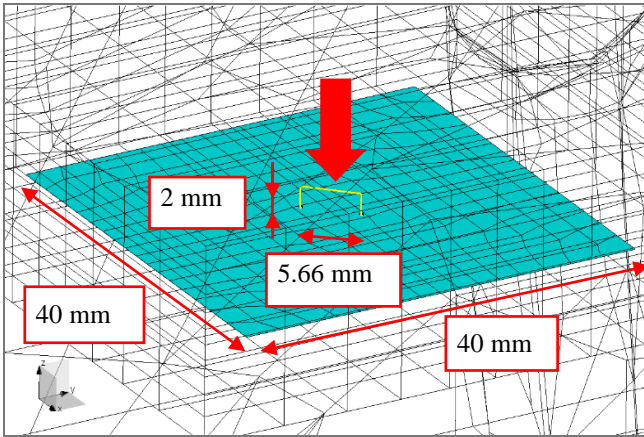


Figure 2. Demonstration model of the circuit board located within the drone.

It can be seen in the Fig. 3 that interior of the drone accommodates the described model of a PCB where onboard electronics is located. In other words, the metallic surface and the half-loop are immersed in the air box inside the drone dielectric.

The S-parameters and 3D radiation pattern¹ of the monopole antenna from Fig. 1 when the drone hovers above the PEC plane are shown in the Fig. 4.

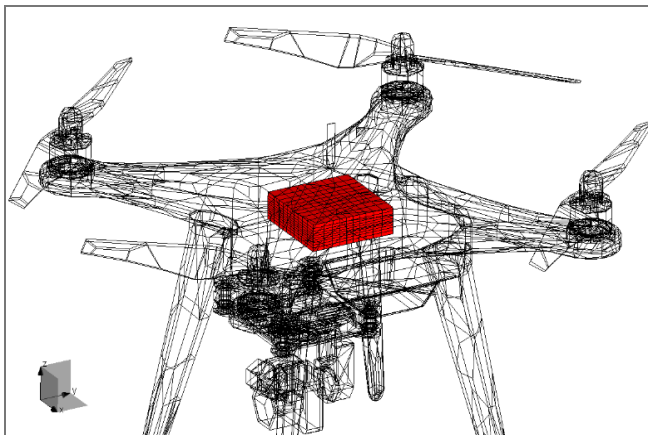


Figure 3. The air box in which the PCB with the half-loop is located.

III. THE MODEL OF THE JAMMER

The simplified model of the jammer in the form of the EM gun only contains a helix antenna and an octagon reflector both located over the PEC ground plane. The details related to geometry of the EM gun structure are

¹ In this paper, all Gain values are in dBi.

presented in the Fig. 5. The center of the antenna reflector is located at the height of 0.1 meter and the axis of the helix is oriented at elevation angle of 35°. The radiation pattern of the jammer antenna above PEC plane is also shown in the Fig. 5. It can be seen that the 3D radiation pattern is influenced by PEC presence and that the position of the antenna has been adjusted to boost the radiation at a sector of interest to a gain higher than 10 dB. The sector of interest covers elevation angles from approximately 9° to approximately 57°.

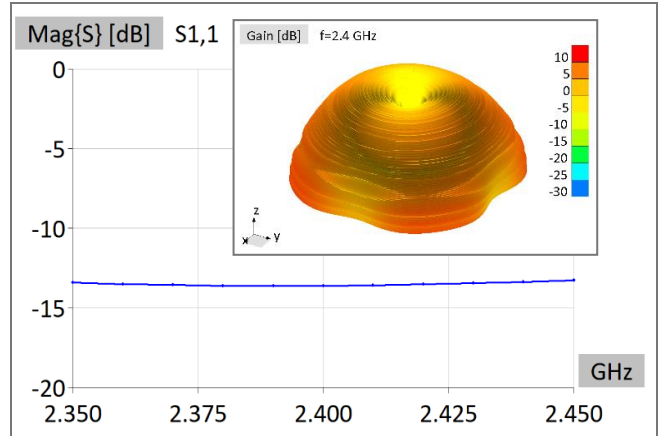


Figure 4. S-parameters and radiation pattern of the monopole mounted on the drone hovering above PEC plane.

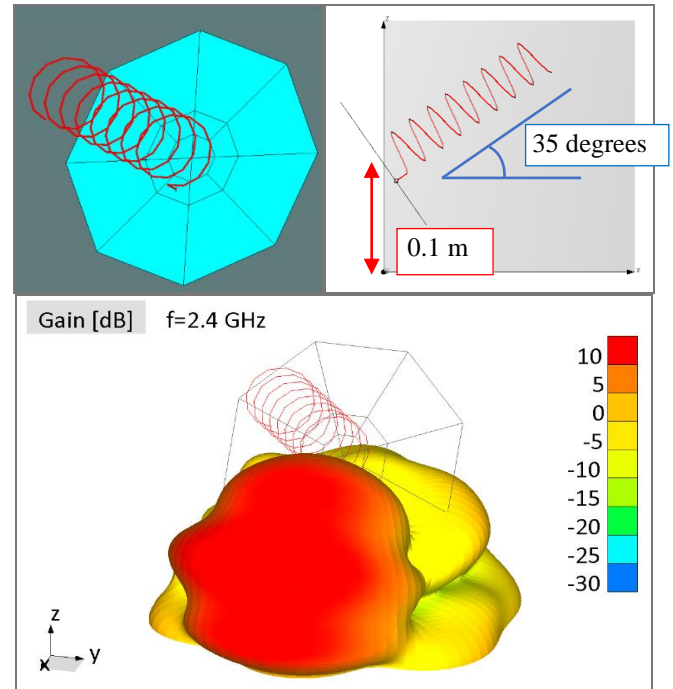


Figure 5. The model and the position of the jammer/EM gun over the PEC plane with 3D radiation pattern at 2.4 GHz.

IV. JAMMING SCENARIO

The particular jamming scenario is illustrated in the Fig. 6 in 3D view, bird’s view, and side view, from top to bottom. Both, drone and anti-drone system are located above the ground modeled as a Perfect Electric Conductor (PEC) plane. It is assumed that the drone flies through the zone protected with the jammer along a straight line, which is a realistic assumption.

The top part of the Fig. 6 shows the direction of the antenna rotation starting from the lowest phi angle ($\phi = 0^\circ$) and the drone flight direction. The middle part of the figure explains the details related to the distance between the antenna and the drone, the angles of antenna rotation, and the drone flight direction. Finally, the lower part of the figure shows the side view of the jamming scenario.

The initial location of the drone is $(x, y, z) = (15 \text{ m}, 0 \text{ m}, 5 \text{ m})$. The final location of the drone is $(x, y, z) = (15 \text{ m}, 25.98 \text{ m}, 5 \text{ m})$. The jammer antenna is located in $(x, y, z) = (0 \text{ m}, 0 \text{ m}, 0.1 \text{ m})$ as shown in Fig. 6 and it is being rotated from $\phi=0^\circ$ to $\phi=60^\circ$ (Fig. 6) keeping the elevation angle of 35° . This means that the monopole antenna mounted on the drone is constantly illuminated with the jammer signal during the described flight along the straight line. The helix antenna which is part of the jammer operates in axial mode at 2.4 GHz (see also Fig. 4 and S_{11} of the monopole antenna mounted on the drone).

Induced current in the middle of the wire located in the root of the monopole antenna mounted on the drone is shown in the Fig. 7. The current induced in the middle of the wire which is part of the half-loop on the PCB is shown in the Fig. 8.

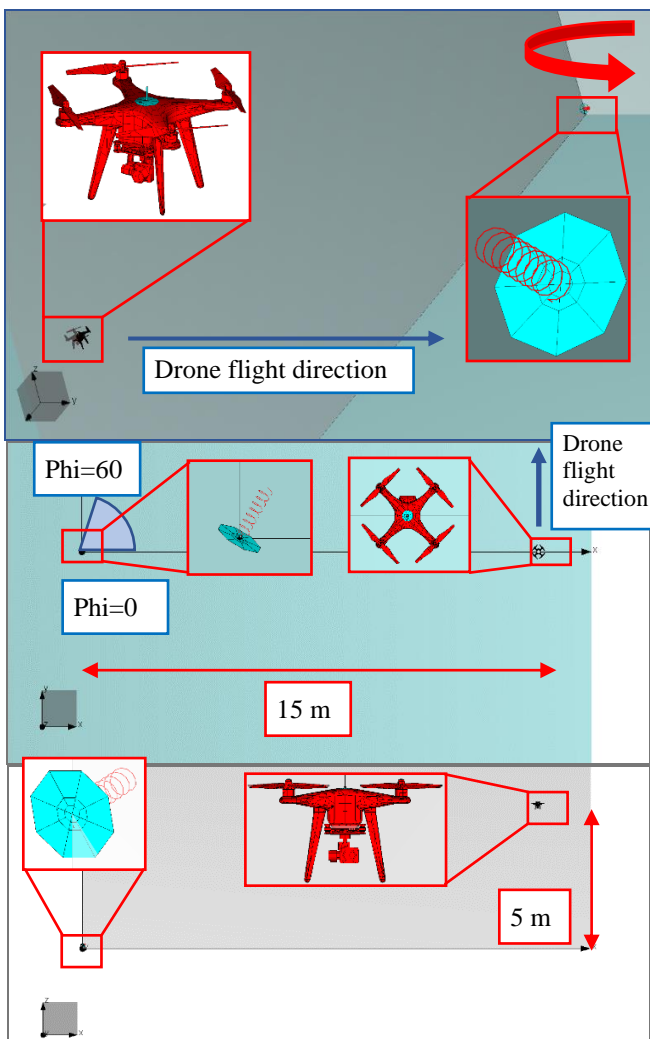


Figure 6. Investigated scenario in 3D, birds view, and side view, from top to bottom, respectively.

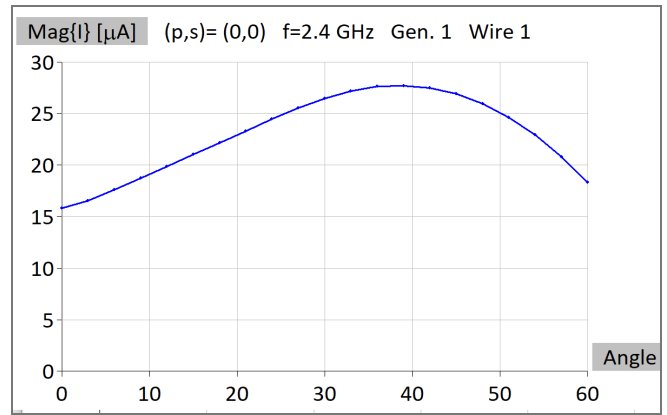


Figure 7. The current induced in the middle of the wire in the root of the monopole antenna.

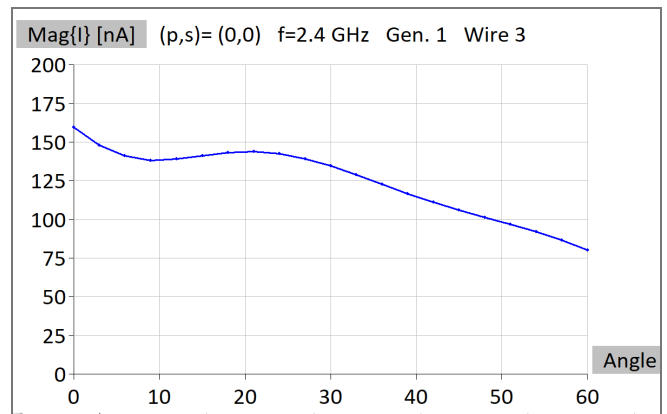


Figure 8. The current induced in the middle of the upper wire in the half-loop on PCB.

V. DECREASING JAMMING EFFECTIVENESS

The presumption of the successful jammer countermeasures is the reliable information of the exact position of the jammer which can be revealed by visual surveillance or EM reconnaissance.

In order to decrease jamming effectiveness, the drone can be modified using a simple, commonly available objects. The PCB area can be easily protected from the outer influence by enclosing it in full (could be a piece of food-wrapping aluminum foil), which is a straight-forward action. However, the antenna used for receiving control signals cannot be fully enclosed for obvious reasons, but, when the position of the jammer is known, it can be partially enclosed so that the covered part coincides with the direction where the jammer is located. The very simple enclosure will be considered here, the one comprising a smooth cylinder or conical object (could be a disposable paper cup). with a metalized part located towards the jammer as described (again, the metallization could simply be a piece of an aluminum foil).

The model of the modified drone is shown in the Fig. 9. The drone dielectric is being displayed in yellow in the upper part of this figure. The cup, with assumed relative dielectric constant of $\epsilon_{rCupReal}=3$ is colored in blue. The metallic sheet representing the aluminum foil is in cyan and clearly visible in both parts of the Fig. 9. Mechanical connections which should be added to real-life drone

structure are excluded from this EM model, without losing the quality of approximation. Enclosing the PCB using thin metal sheet following a box shape displayed in Fig. 3 can be noticed in the lower part of the Fig. 9. More precise explanation of the scenario with metallic sheet is presented in Fig. 10 where the arrow points to the cup which is mounted on the top of the drone. In other words, the metallic sheet is positioned on the left side of the cup.

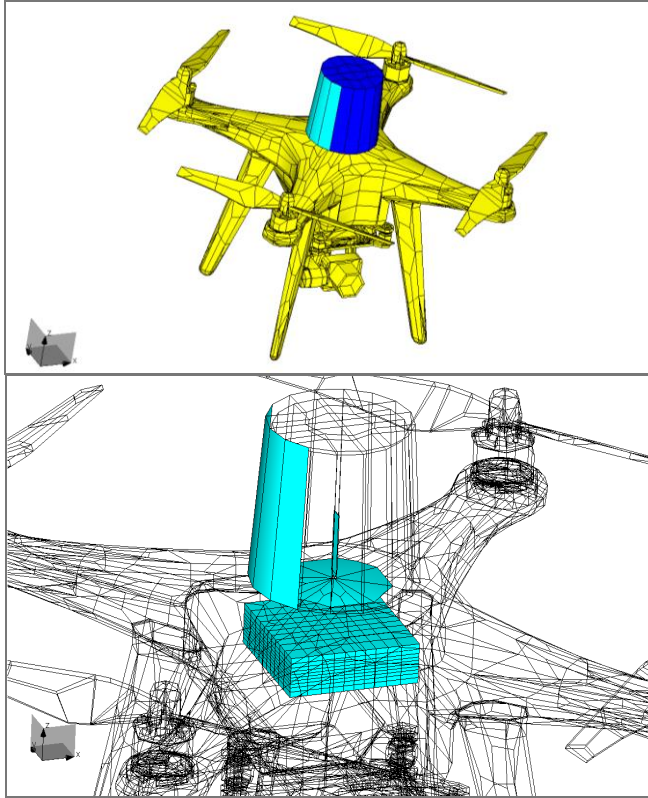


Figure 9. The drone with modifications and the metallic parts with enclosing of PCB.

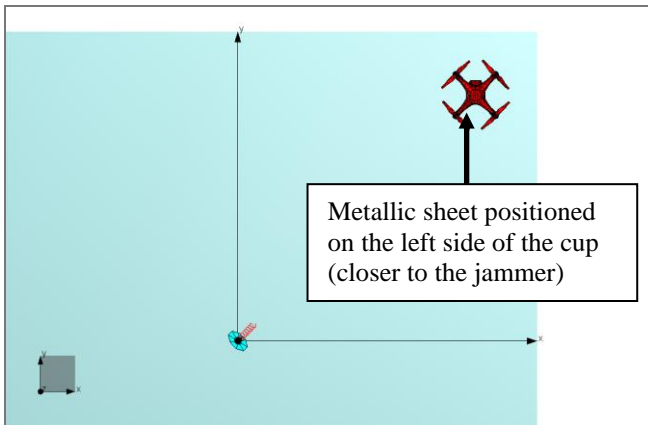


Figure 10. The position of the drone and the jammer with explained position of the metallic sheet. Not to be scaled.

The output results are displayed and compared in Figs 11-12. Fig. 11 displays comparison of the induced currents on the wire in the root of the antenna without the cup, with the cup and metallic sheet, and with the metallic sheet, only. It can be seen that without the metallic sheet attached to the cup, the level of induced current is the highest. Adding metallic sheet wrapped around the cup lower levels of

induced currents are obtained. Similar result appears with the metallic sheet added and without the cup. This proves that metallic sheet mainly influences the jamming signal.

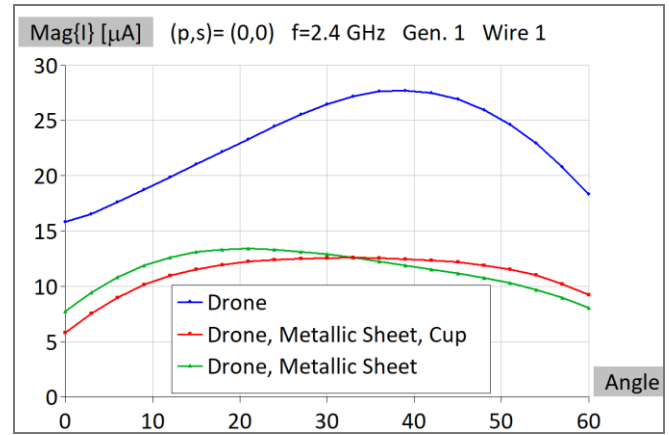


Figure 11. The comparison of currents induced in the middle of the wire in the root of the monopole antenna.

Fig. 12 displays comparison of currents on the PCB wire in three previously explained cases. The drop in level of the induced signal for shielded PCB is clearly noticeable.

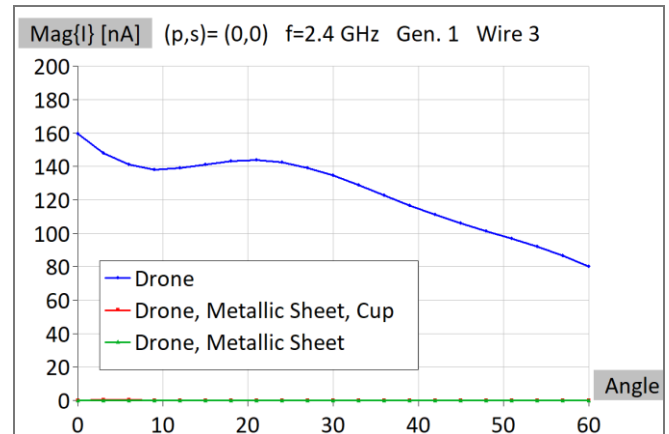


Figure 12. The comparison of currents induced in the middle of the upper wire in the half-loop on PCB

VI. COMPUTER PLATFORM AND SIMULATION TIME

All scenarios were simulated using a MoM based software and dedicated sweeping tool rotating the jammer from angle $\phi=0^\circ$ to $\phi=60^\circ$ in 21 equidistant points and moving the drone in the appropriate direction. The most demanding simulation of the jammed drone with the metallic sheet and the cup required 16,761 elements and 36,060 unknowns. The simulation time per a single angle of rotation for the same model is about than 8 minutes. The computer used for carrying out the simulation is Intel® Xeon® Gold 5118 CPU @ 2.30GHz (2 processors) with 192 GB RAM and a GPU card NVIDIA GeForce GTX 1080 Ti. GPU card is used for both matrix fill-in and matrix inversion.

VII. CONCLUSION

A scenario encompassing the drone and an anti-drone system in the form of an EM gun over the PEC ground plane has been investigated. The effectiveness of jamming is demonstrated by calculating the induced currents at 2.4 GHz. Also, basic countermeasures were presented based on simple modifications of the drone.

The main effect of the jamming comes from the saturation of the receiver. Such a result can be explained easily as the antenna is directly exposed to the jamming signal. It was shown that mounting metallic sheet between the jammer and the receiving monopole, using an auxiliary cylindrical object like a paper cup, can significantly reduce the effectiveness of the jammer signal.

The current induced in the PCB elements might cause malfunction of drone electronics but being significantly lower than the level of the current on the antenna connection, is of secondary importance to the jamming scenario. Furthermore, the countermeasures can be performed easier by enclosing critical area around the PCB.

As it has been confirmed that simple countermeasures can

make the drone resilient to jamming from a single source, the counter-countermeasures should include the distribution of several jammers in different locations around the target as it makes the method of partial shielding impractical.

Utilization of a Method-of-Moments (MoM) based software, for calculation of the induced currents has been also demonstrated. The numerical results have been obtained with high efficiency on an affordable desktop machine.

Further investigation could include propagation effects, or adding some objects such as metallic fences or lampposts and their influence on jammer-to-drone link.

REFERENCES

- [1] D. M. Pozar, *Microwave Engineering*, 2nd ed., USA, John Wiley & Sons, 1998.
- [2] D. Banjac, *Electronic Warfare in Anti-Aircraft Defense* (in Serbian), Military Publishing and Media Center, Belgrade, 1986.
- [3] J. L. Volakis, *Antenna Engineering Handbook*, 4th ed., USA: McGraw-Hill, 2007
- [4] WIPL-D Software, WIPL-D d.o.o, Belgrade 2021. www.wipl-d.com
- [5] B. M. Kolundzija, A. R. Djordjevic, *Electromagnetic Modeling of Composite Metallic and Dielectric Structures*, 1st ed. Norwood, Massachusetts, USA: Artech House, 2002.

Simulation Study of Voxel-Based Head Phantom for Medical Microwave Imaging

Mladjen Stevanetic, Branko Kolundzija, Tushar Singh, Marija Nikolic Stevanovic

Abstract—The paper describes the crucial role of phantoms in Microwave Imaging (MWI) for medical devices. Accurate modelling of numerical scenarios is crucial in designing, testing, and developing MWI devices. Phantoms with appropriate tissue electrical properties are inevitable components of imaging scenarios. Therefore, high computing resources are required to develop such phantom, and EM simulation of such scenarios requires a more prolonged time. A defined blueprint is required to reduce the complexity of such scenarios to use them effectively for MWI purposes. In the given paper, a brief study of the three-dimension voxel model of the head is presented, where a unit cell is a cube with tissue-mimicking properties. The phantom is developed on the WIPL-D Pro EM simulation platform. Further, the voxels are grouped in the form of $N \times N \times N$, where N is the number of voxels on each axis. Homogenization techniques are implemented on the grouped voxels and result in one big cube, the main building element of the electromagnetic model. The RCS simulation is performed with plane wave excitation for different values of N , and the results are analyzed for convergence to the reference model. Also, the relative mean absolute deviation (RMA) of the whole phantom as a result of the homogenization process is presented and its convergence is compared with the convergence of the mean deviation of simulated results.

Index Terms—Head phantom; Microwave Imaging; Voxel Model; Zubal

I. INTRODUCTION

BRAIN stroke has been one of the leading causes of death in humans over the last decade. Early-stage screening of stroke is a crucial step for diagnosis and treatment purposes [1]. Conventional technologies such as MRI, CT and X-ray are the gold standard for stroke detection due to accurate scanned results with high spatial resolution for clinical diagnosis. Although, these methods have several disadvantages, such as expensive procedures, low portability and ionizing radiation [2] – [3]. On the other hand, Microwave Imaging (MWI) is envisioned as a complementary tool to the imaging technologies for brain stroke detection. It is a low health risk, non-invasive, and cost-effective procedure [4] – [5].

Developing medical devices based on microwave imaging requires accurate electromagnetic modelling of imaging scenarios. The vital components of imaging scenarios are powerful EM simulation environment, anthropomorphic

Mladjen Stevanetic is with WIPL-D d.o.o. Belgrade, Serbia (e-mail: mladjen.stevanetic@wipl-d.com)

Branko Kolundzija is with WIPL-D d.o.o. Belgrade, Serbia and School of Electrical Engineering, University of Belgrade, Serbia (e-mail: branko.kolundzija@wipl-d.com).

Tushar Singh is with WIPL-D d.o.o. Belgrade, Serbia and School of Electrical Engineering, University of Belgrade, Serbia (e-mail: tushar.singh@wipl-d.com).

Marija Nikolic Stevanovic is with School of Electrical Engineering, University of Belgrade, Serbia (e-mail: mnikolic@etf.bg.ac.rs).

phantoms, tissue electrical properties and a measurement system. The simulation tool provides ease in modelling and accurate numerical analysis. The measurement system reduces to the antenna system around the organ of interest. Tissue mimicking properties help to understand the wave propagation through the human organ. Realistic human-like phantoms are crucial to understanding the complex structure of the organ with defined electrical properties. Modelling complex phantoms is the decisive factor for the accuracy and validation of the imaging scenario. Voxel and STL formats are widely available for designing phantoms [6]. The source format of the phantom is highly complex and requires efficient strategies to reduce the complexity of the structure while retaining accuracy.

The proposed study is focused on the study and accurate design of voxel based anatomically realistic head phantom for MWI purposes. The phantom data is usually derived from MRI images. The model is obtained from an online repository [7] in binary format. The 3D EM simulation platform WIPL-D Pro helps to transform the medical data into the 3D electromagnetic head model [8]. The unit structure of the actual phantom is a voxel or small cube with a side length of approximately 1 mm. The source file contains around 4 million such voxels. Each voxel has its own defined tissue properties. Simulation of such a model is very challenging. Therefore, with efficient procedures, the complexity is reduced. The voxels are grouped to form a big cube and then homogenization techniques are implemented on these big cubes. As mentioned, each voxel defined with one cube leads to a huge requirement of resources, therefore at the initial stage voxels are grouped using the parameter N , where N denotes the total number of voxels along each axis. The reference model is created with $N=3$. The homogenization is implemented using various mixing formulas [9]. A group of voxels with the given value of N is treated as one big cube, and its electrical property is derived from the averaging techniques. Implementing these methods significantly reduces the computational requirement and speeds up the simulation for EM analysis within the measurement system. In order to study the agreement between homogenization techniques and reduction in complexity, EM simulation is performed for various values of N ranging from 3 to 12 voxels in each axis. The excitation is a plane wave for the bistatic RCS estimation. The deviation between the reference model and the model with higher values of N gives the information on the accuracy of the simplification process in terms of % error. At the same time, the Relative Mean Absolute (RMA) differences between the reference model and other models (with $N>3$) give insight in the averaging process and its convergence.

The paper is divided into three main sections. Section II is about the voxel model and homogenization techniques,

Section III is focused on numerical results, and Section IV concludes the paper.

II. VOXEL PHANTOM AND HOMOGENIZATION

A. Voxel phantom

The voxel phantom represents dispersive dielectric properties data of a part of the human body (organ(s)), as a result of the MRI (Magnetic Resonance Imaging) or CT (computed tomography x-ray) scans of respective human body part [7].

That scan outputs the grid of points, named voxels, distributed in three-dimensional volume that covers the scanned organ with a specific resolution. Each voxel brings different dielectric properties of tissue. Although some phantom use Cole-Cole and Debye parameters to present dielectric properties of the tissue [10] - [11], this type of phantom comes with the binary input that holds identifications of tissue types for each voxel. The number of voxels varies depending on organ size and scanning resolution from 2 to 20 million or more. The resolution or distance between voxels is considered around 0.5 mm or 1 mm. Some of the voxels contain information on the surrounding media, in our case it is air.

However, it is very challenging and still under research to simulate the entire model with millions of unknowns, defined with thousands of domains i.e., closed regions with the same dielectric properties. Today's most robust full MoM solver, WIPL-D, reinforced with the HOBFs and fully parallelized, still requires large simulation time for millions of unknowns. Therefore, we designed a simple procedure, built-in WIPL-D, for transforming the medical data to the electromagnetic model being simulated in a reasonable amount of time and providing valuable information for overall phantom analysis.

B. Homogenization

All the voxels are treated as small cubic volumes in space with specific dielectric constant values. Generally, these values are different for different voxels but are similar for the voxels of the same tissue type. In order to decrease the complexity of such a significant problem, we perform the averaging techniques on voxels. We create bigger cubic volumes that contain several voxels, taking the same number of voxels per each of the coordinate axes of a new, larger volume. If we treat one voxel as a small cube with a size equal to the resolution of the phantom, we create a big cube with N voxels per axis. Fig. 1 shows a preview of the Zubal head phantom [7] in two resolutions $N=3$ and $N=8$ on the WIPL-D Pro platform.

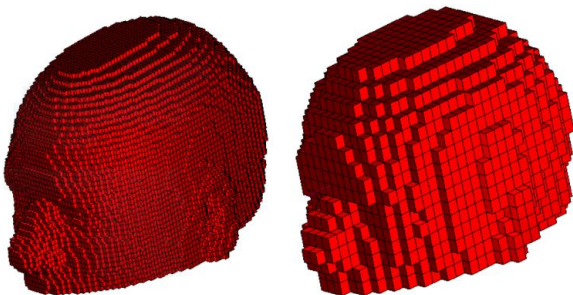


Fig. 1. Zubal anthropomorphic head phantom. Left, resolution $N=3$ and right, resolution $N=8$.

By increasing N , the resolution and therefore the complexity is gradually decreased, but the error due to averaging procedure is increased.

The new, big cube, represents a building element of the electromagnetic model. Its effective permittivity is obtained using mixing or averaging formulas applied to all the dielectric constant values of the voxels inside the same cube. These formulas were initially implemented for physical mixtures.

Standard averaging formula implements standard arithmetic mean:

$$\epsilon_{\text{eff}} = \frac{\sum_{i=1}^{N^3} v_i \cdot \epsilon_i}{\sum_{i=1}^{N^3} v_i}, \quad (1)$$

where ϵ_i is voxel dielectric constant and v_i is voxel volume.

Lichtenecker formula is a logarithmic formulation of physical components of the mixture as shown below:

$$\ln(\epsilon_{\text{eff}}) = \frac{\sum_{i=1}^{N^3} v_i \cdot \ln(\epsilon_i)}{\sum_{i=1}^{N^3} v_i}. \quad (2)$$

The formula has been established for biological materials such as human blood [12].

Looyenga equation is considered to be the most reliable formulation to predict the effective permittivity of the mixture [13] - [14]:

$$\epsilon_{\text{eff}}^{\left(\frac{1}{M}\right)} = \frac{\sum_{i=1}^{N^3} v_i \cdot \epsilon_i^{\left(\frac{1}{M}\right)}}{\sum_{i=1}^{N^3} v_i}, \quad (3)$$

where $M = 2, 3$. Looyenga equation is considered up to third degree. All the formulas were implemented and the results of conversion of the phantom to the electromagnetic model as well as simulated results, and its comparison, were provided for each of the formulas. That is given in the next section.

Once the effective dielectric constant that represents averaged value of all the voxels permittivity inside a big cube is obtained, the second level of homogenization is applied. It implies all the big cubes being considered to define a finite number of the domains. Hence the number of big cubes is still significant, for example, more than 100000 in some cases, each cube cannot represent a separate domain. Therefore, all the cubes are divided into several groups, where, inside each group, a relative deviation of the effective dielectric constant is kept below some small threshold. In other words, the cubes in the group possess similar values of effective dielectric constant. One group defines one domain. The domain dielectric constant is a mean value of all effective dielectric constants within the group. The domain dielectric constant is assigned to all the cubes in the group as their new averaged value (new effective dielectric constant) because it is used in the electromagnetic simulation of the phantom. We called it "the assigned dielectric constant".

The number of the domains approximately goes from 100 to 300 for all the resolutions and all four mixing formulas considered in the paper. The higher the resolution (lower N)

the number of domains generally decreasing and approaches to the number of different tissue types in the model. Each domain represents a closed region, and all the mesh elements, or big cubes' sides, inside the domain were removed to reduce complexity and thus the number of unknowns in the final model. Only domains' surface mesh elements took part in the MoM simulation.

The last part of big cubes' creation is the calculation of the deviation. For each cube, the deviation is calculated per the above-mentioned formulas. The formula used for averaging is also used for calculating deviation. The only difference is that part ε_i in the above equations is changed with the $|\varepsilon_i - \varepsilon'_{\text{eff}}|$ which is the deviation of one small voxel. Therefore, the Lichtenecker method is given as

$$\ln(\delta) = \frac{\sum_{i=1}^{N^3} v_i \cdot \ln |\varepsilon_i - \varepsilon'_{\text{eff}}|}{\sum_{i=1}^{N^3} v_i}, \quad (4)$$

standard and Looyenga method is

$$\delta\left(\frac{1}{M}\right) = \frac{\sum_{i=1}^{N^3} v_i \cdot |\varepsilon_i - \varepsilon'_{\text{eff}}|^{\left(\frac{1}{M}\right)}}{\sum_{i=1}^{N^3} v_i}, \quad (5)$$

where $M = 1, 2, 3$, v_i is voxel volume and $\varepsilon'_{\text{eff}}$ is the assigned dielectric constant value.

Therefore, a mean deviation for each big cube is calculated as the mean absolute distance of each voxel in the cube from the assigned dielectric constant value, rather than the distance from the averaged value ε_{eff} .

C. Estimation of Error

In the end, the deviation for the whole phantom is obtained from the particular deviations of big cubes. This value actually represents the error raised from the averaging procedure.

The error value is also calculated using a specific formula which is similar to the averaging process, so, either with standard, Lichtenecker or Looyenga procedure. Lichtenecker method

$$\ln(\Delta) = \frac{\sum_{j=1}^K V_j \cdot \ln(\delta_j)}{\sum_{j=1}^K V_j}, \quad (6)$$

standard and Looyenga method

$$\Delta\left(\frac{1}{M}\right) = \frac{\sum_{j=1}^K V_j \cdot \delta_j^{\left(\frac{1}{M}\right)}}{\sum_{j=1}^K V_j}, \quad (7)$$

where K is number of big cubes, $M = 1, 2, 3$, δ_j is the big cube deviation and V_j is big cube volume. We can calculate the average value A of the whole phantom using the Lichtenecker method

$$\ln(A) = \frac{\sum_{j=1}^K \sum_{i=1}^{N^3} v_{ji} \cdot \ln |\varepsilon_{ji}|}{\sum_{j=1}^K \sum_{i=1}^{N^3} v_{ji}}, \quad (8)$$

standard and Looyenga method

$$A\left(\frac{1}{M}\right) = \frac{\sum_{j=1}^K \sum_{i=1}^{N^3} v_{ji} \cdot |\varepsilon_{ji}|^{\left(\frac{1}{M}\right)}}{\sum_{j=1}^K \sum_{i=1}^{N^3} v_{ji}}, \quad (9)$$

where K is number of big cubes, $M = 1, 2, 3$, v_{ji} is voxel volume of i -th voxel in the j -th big cube and ε_{ji} is voxel dielectric constant of i -th voxel in the j -th big cube. The air voxels are omitted from the overall phantom.

Now, we can calculate the relative mean absolute error of the whole phantom as

$$\text{RMA}[\%] = \frac{\Delta}{A} * 100. \quad (10)$$

This value is provided at the end of the conversion process of the phantom to the electromagnetic model, ready for simulation.

The relative mean absolute deviation of simulated results is given by

$$\text{RMA}_{\text{sim}}[\%] = \frac{\frac{1}{n} \cdot \sum_{i=1}^n |E_i^N - E_i^{\text{Ref}}|}{\frac{1}{n} \cdot \sum_{i=1}^n |E_i^{\text{Ref}}|} * 100, \quad (11)$$

where n is the number of directions for bistatic RCS far-field, here 73×37 for azimuth and elevation, E_i^N is far-field for phantom with resolution N and E_i^{Ref} is far-field for the reference phantom.

III. RESULTS

We used the Zubal head phantom for analysis. The full MoM electromagnetic simulations were performed in WIPL-D software.

Simulations in WIPL-D provide results for bistatic RCS in a number of space angles, with plane wave excitation. The results were provided for different resolutions $N=3, 4, \dots, 12$ and for all mixing formulas, Lichtenecker and Looyenga where $M=1, 2, 3$. We also provide the *RMA* values for all the conversions.

The phantom with the highest resolution, $N=3$, is taken as the reference result. At the operating frequency of 1 GHz, this phantom has 500000 unknowns with around 100 domains and the resolution is about 3.5 mm. Simulation time on the machine Intel(R) Xeon(R) CPU E5-2650 v4 @ 2.20GHz (2 processors), with 48 logical processors, 256 GB of RAM and 4 GPU cards NVIDIA GeForce GTX 1080Ti, is about 7.3 hours.

All other phantoms were compared to this reference phantom, mean deviation of the RCS far-field is calculated for each of them relative to the reference phantom i.e., *RMA_{sim}*. In the same manner, the differences were provided for the *RMA* values too, relative to the reference phantom.

The next four figures present a comparison of *RMA_{sim}* and *RMA* relative to the reference phantom.

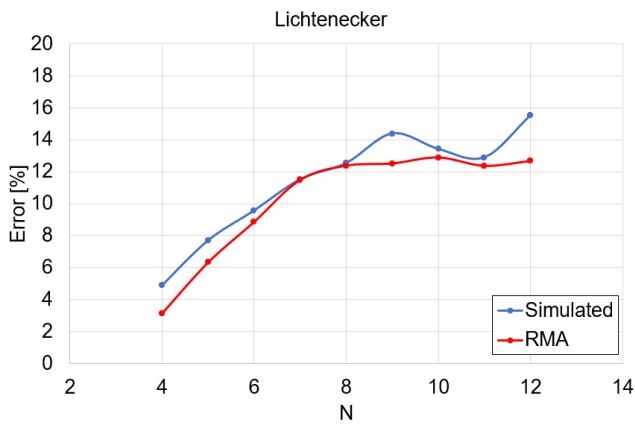


Fig. 2. Lichtenecker method. The Error for the blue trace represents the mean deviation of the RCS far-field relative to the reference phantom $N=3$ i.e., RMA_{sim} . The Error for the red trace represents differences in RMA also relative to the reference phantom $N=3$. N is resolution.

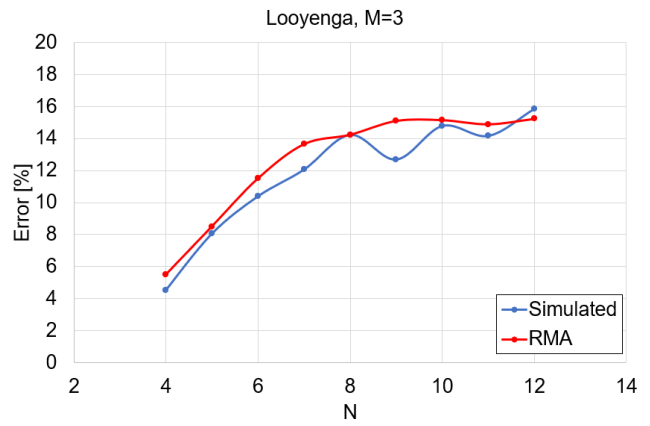


Fig. 5. Looyenga method, with $M=3$ degree. The Error for the blue trace represents the mean deviation of the RCS far-field relative to the reference phantom $N=3$ i.e., RMA_{sim} . The Error for the red trace represents differences in RMA also relative to the reference phantom $N=3$. N is resolution.

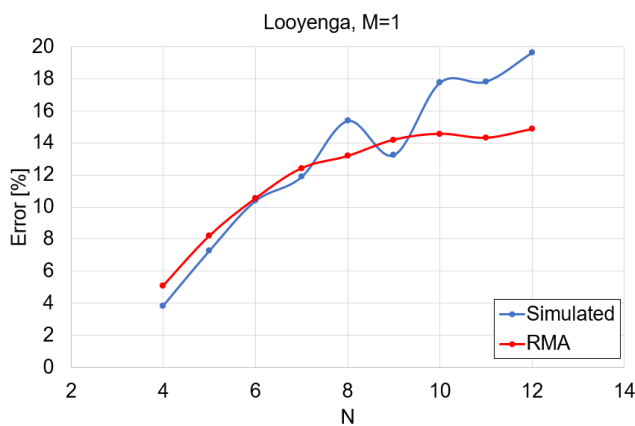


Fig. 3 Looyenga method, with $M=1$ degree. The Error for the blue trace represents the mean deviation of the RCS far-field relative to the reference phantom $N=3$ i.e., RMA_{sim} . The Error for the red trace represents differences in RMA also relative to the reference phantom $N=3$. N is resolution.

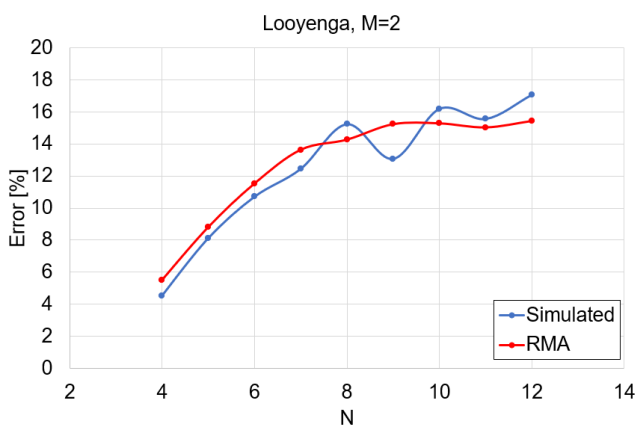


Fig. 4. Looyenga method, with $M=2$ degree. The Error for the blue trace represents the mean deviation of the RCS far-field relative to the reference phantom $N=3$ i.e., RMA_{sim} . The Error for the red trace represents differences in RMA also relative to the reference phantom $N=3$. N is resolution.

IV. CONCLUSION

We present a novel technique for the conversion of large voxel phantoms by averaging and homogenization of the voxel data to the electromagnetic simulation ready model. The obtained model is suitable for analysis of the imaging scenario, with reasonable simulation time.

We've also shown the estimated error, or relative mean absolute value RMA , as a result of the simplification process. A comparison in error behavior between RMA and simulated RCS results is provided. It can be seen that the RMA expresses very similar behavior with the mean deviation in simulated results, for different resolutions, relative to some phantom of a very high resolution taken as the reference. The estimated convergence of the RMA can serve as a guide of anticipating the characteristics of the phantom before performing electromagnetic simulation itself.

REFERENCES

- [1] S. Mustafa, B. Mohammed and A. Abbosh, "Novel Preprocessing Techniques for Accurate Microwave Imaging of Human Brain," in IEEE Antennas and Wireless Propagation Letters, vol. 12, pp. 460-463, 2013
- [2] A.S. M. Alqadami, A. Trakic, A. E. Stancombe, B. Mohammed, K. Bialkowski and A. Abbosh, "Flexible Electromagnetic Cap for Head Imaging," in IEEE Transactions on Biomedical Circuits and Systems, vol. 14, no. 5, pp. 1097-1107, Oct. 2020, doi: 10.1109/TBCAS.2020.3025341.
- [3] Zhao Wang, Eng Gee Lim, Yujun Tang, Mark Leach, "Medical Applications of Microwave Imaging", The Scientific World Journal, vol. 2014, Article ID 147016, 7 pages, 2014. <https://doi.org/10.1155/2014/147016>.
- [4] M. Pastorino, A. Randazzo, Microwave Imaging Methods and Applications, in Artech House, 2018.
- [5] L. Crocco, I. Karanasiou, M. James, R. Conceição, "Emerging Electromagnetic Technologies for Brain Diseases Diagnostics, Monitoring and Therapy," Springer, Cham, Switzerland, 2018.
- [6] S. N. Makarov, G. M. Noetscher and A. Nazarian, Low-Frequency Electromagnetic Modeling for Electrical and Biological Systems Using Matlab, John Wiley & Sons, Inc, 2016
- [7] The Zubal Phantom – <http://noodle.med.yale.edu/zubal/>
- [8] WIPL-D software suite (WIPL-D Pro v17 & Pro CAD 2020), WIPL-D d.o.o, Belgrade, 2020.
- [9] T. Singh, M. Stevanetic, M. Stevanovic and B. Kolundzija, "Homogenization of Voxel Models using Material Mixing Formulas," 2020 14th European Conference on Antennas and Propagation (EuCAP), 2020, pp. 1-4.
- [10] Zastrow E, Davis SK, Lazebnik M, F. Kelcz, B. D. Van Veen, and S. C. Hagness, Database of 3D grid-based numerical breast phantoms for

use in computational electromagnetics simulations. Madison (WI): University of Wisconsin-Madison; c2014. [cited 2014 Sep 21]. Available at: <https://uwcem.ece.wisc.edu/phantomRepository.html>.

- [11] M. Lazebnik, L. McCartney, D. Popovic, C. B. Watkins, M. J. Lindstrom, J. Harter, S. Sewall, A. Magliocco, J. H. Booske, M. Okoniewski, and S. C. Hagness, "A large-scale study of the ultrawideband microwave dielectric properties of normal breast tissue obtained from reduction surgeries," *Physics in Medicine and Biology*, vol. 52, pp. 2637-2656, April 2007.
- [12] Ray Simpkin, "Derivation of Lichtenecker's Logarithmic Mixture Formula From Maxwell's Equations," *IEEE Transactions on Microwave Theory and Techniques*, Vol. 58, No. 3, March 2010.
- [13] S.O. Nelson, "Measurement and Computation of Powdered Mixture Permittivities," *Proceedings of the 17th IEEE Instrumentation and Measurement Technology Conference*, DOI: 10.1109/IMTC.2000.848661.
- [14] Kimmo Kalervo Kärkkäinen, Ari Henrik Sihvola, and Keijo I. Nikoskinen, "Effective Permittivity of Mixtures: Numerical Validation by the FDTD Method," *IEEE Transactions on Geoscience and Remote Sensing*, Vol. 38, No. 3, May 2000 1303.

Radome Shape Impact on Automotive Radar Sensor Operating at 79 GHz

Nebojša Pupavac and Miodrag Tasić, *Member, IEEE*

Abstract—At high frequencies radome (Radar Dome) degrades the automotive radar performance significantly. To gain better understanding of this phenomenon the radome shape and its impact on radiation pattern of the radar antenna array is analyzed in this paper. To analyze the impact of the radome shapes, an array of printed antennas is simulated with two different radome shapes and compared against the radiation pattern simulated without any radome. A simple single patch antenna for 79 GHz is designed using WIPL-D software platform, which was used for simulation of the antenna array with and without radome.

Index Terms—Radome; radar sensor; antenna array; patch antenna.

I. INTRODUCTION

A radome (radar dome) is a protective shield that encloses mmWave radar sensors and the antenna. It protects the antennas and electronics from external environment effects. The radome should be designed to minimally attenuate the electromagnetic signals transmitted and received by the antennas and as such should effectively be transparent to radio waves.

Since short range automotive radars work in 77-81 GHz frequency range [1], wavelengths of radar signals are rather small (3.75 mm at 80 GHz). This can cause significant interactions between radar signals and the plastic parts of the vehicle (painted bumper) and/or used radome, resulting in unpredictable error in the angle of arrival estimation [2]. Sometimes a calibration of the system can include the radar itself [3], but in the most cases radome is designed separately, with a goal to minimize reflections [4].

Although there are some general guidelines for automotive radar design [5], an electromagnetic simulation is necessary step in this process. In this paper we present results of the electromagnetic simulations for two radomes scenarios: spherical radome and rectangular radome, covering microstrip patch array. We will compare radiation patterns of these two systems with the radiation pattern of the microstrip patch array without the radome. The results can be used as a starting point in finding the optimal radome shape for a particular automotive radar design.

Nebojša Pupavac is with the School of Electrical Engineering, University of Belgrade, 73 Bulevar kralja Aleksandra, 11020 Belgrade, Serbia (e-mail: nebojsapupavac@gmail.com), (<https://orcid.org/0000-0001-7851-7649>)

Miodrag Tasić is with the School of Electrical Engineering, University of Belgrade, 73 Bulevar kralja Aleksandra, 11020 Belgrade, Serbia (e-mail: tasic@etf.bg.ac.rs), (<https://orcid.org/0000-0002-8356-1190>)

II. GUIDELINES FOR RADOME DESIGN

Since the most radomes are designed out of perfect dielectric material (with the relative permeability equal to 1, and the conductivity which is close to 0), main parameters for selecting appropriate material are relative permittivity and the loss tangent. The lower loss tangent provides the smaller attenuation by the radome, and overall smaller effect of the radome on the antenna performance. In finding optimal relative permittivity and a shape of the radome, the electromagnetic theory of time-harmonic electromagnetic fields for the plane-wave assumption can be used.

Electromagnetic wave reflections occur at the boundaries of the plane of mismatch. The plane of mismatch is the boundary of two domains with different dielectric permittivity. The interaction of the electromagnetic wave at the boundaries leads to the reflection and transmission of waves, quantized in terms of reflection coefficient R ,

$$R = \frac{\sqrt{\epsilon_{r1}} - \sqrt{\epsilon_{r2}}}{\sqrt{\epsilon_{r1}} + \sqrt{\epsilon_{r2}}}, \quad (1)$$

and transmission coefficient T ,

$$T = \frac{2\sqrt{\epsilon_{r1}}}{\sqrt{\epsilon_{r1}} + \sqrt{\epsilon_{r2}}}. \quad (2)$$

Expressions (1) and (2) hold for an incident plane wave normal to the infinite flat boundary between the domains with relative permittivities ϵ_{r1} and ϵ_{r2} [6]. These expressions indicate that lower relative permittivity of radome dielectric material causes lower degradation of radar performance (since the other domain is air, with relative permittivity close to 1). However, optimal radome material needs to provide adequate mechanical characteristics, and the boundary in the general case is not a flat surface. Therefore, the selection of the dielectric material is always a tradeoff.

The radome thickness is particularly important for optimal performance of the automotive radar sensors. To avoid reflection at the radome wall, its thickness should be equal to an integer multiple, n , of the half of the wavelength in the radome [6]:

$$t_{\text{opt}} = n \frac{c_0}{2f_r \sqrt{\epsilon_r}}, \quad (3)$$

where c_0 is speed of light in vacuum, ϵ_r is relative permittivity of radome material, and f_r is central frequency.

Typical parameters for the radome materials are shown in Table I. For radome shape analyses PTFE is selected as optimal solution which could be fabricated and tested to confirm simulation results presented in this paper. For $\epsilon_{rPTFE} = 2$ and $f_r = 79$ GHz, the optimal thickness of radome material from (3) is obtained for $n = 2$, $t_{opt} = 2.68$ mm (since the radome has to be at least 2 mm thick). Note that (3) is valid for electromagnetic plane waves at infinite flat boundary.

TABLE I
TYPICAL RADOME MATERIALS

Material	Relative Permittivity (ϵ_r)	Loss tangent $tg(\delta)$
Polycarbonate	2.9	0.012
ABS	2.0-3.5	0.0050-0.019
PEEK	3.2	0.0048
PTFE	2	<0.0002
Plexiglass	2.6	0.009
PE	2.3	0.0003
PBT	2.9-4.0	0.002

The optimal distance between the antenna and the internal surface of the radome helps to minimize the effects of reflections caused by the radome. These effects become minimal if the waves returned to the antenna are in phase with the transmitted waves. So, the optimal distance between antenna and radome is [5]:

$$d_{opt} = m \frac{c_0}{2f_r}. \quad (4)$$

For $m = 7$ we have $d_{opt} = 13.29$ mm. A spherical radome in that case would have inner diameter of 26.58 mm, which is sufficient to cover the whole automotive radar sensor, including all necessary components.

III. ANTENNA DESIGN

We will model typical automotive radar sensors at 79 GHz, with four microstrip patch antennas. The layout of the single patch antenna is shown in Fig. 1. A substrate thickness is $t = 127 \mu\text{m}$, with relative permittivity $\epsilon_r = 3$, and loss tangent $\tan \delta = 0.0017$.

The patch width (W) and length (L) are calculated using the standard approximation [7],

$$W = \frac{c_0}{2f_r \sqrt{\frac{\epsilon_r + 1}{2}}}, \quad (5)$$

$$L = \frac{c_0}{2f_r \sqrt{\epsilon_{eff}}}, \quad (6)$$

where ϵ_{eff} is given by

$$\epsilon_{eff} = \frac{\epsilon_r + 1}{2} + \frac{\epsilon_r - 1}{2} \left(1 + 12 \frac{t}{W} \right)^{-\frac{1}{2}}. \quad (5)$$

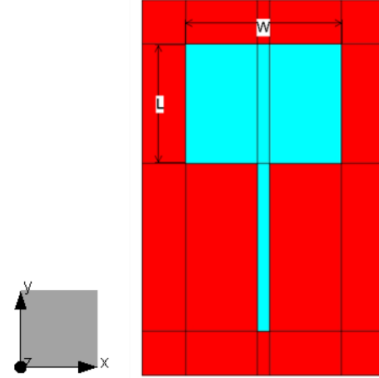


Fig. 1. Single rectangular patch antenna.

Antenna matching is achieved by adjusting the length of 0.1 mm wide feeding line using software package for electromagnetic modeling WIPL-D Pro [8]. Parameter s_{11} over desired frequency bandwidth is shown in Fig. 2, whereas radiation pattern in H-plane and E-plane is shown in Fig. 3.

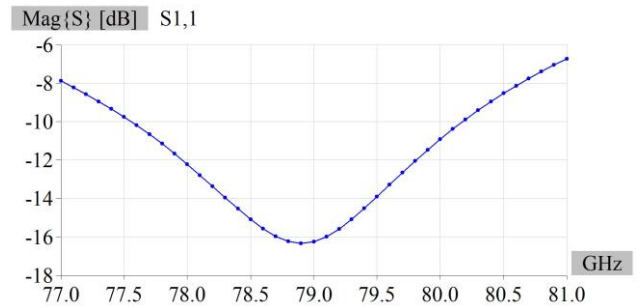


Fig. 2. Parameter s_{11} for a single microstrip patch antenna.

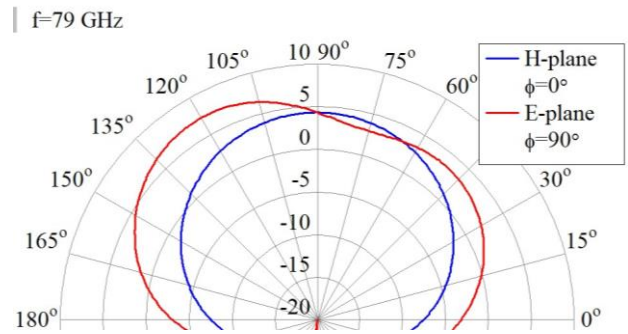


Fig. 3. Radiation pattern (Gain in dB) for a single microstrip patch antenna.

Typical automotive radar sensors at 79 GHz are using 3 Tx and 4 Rx antennas. In this simulation only Rx antenna is simulated. It is made of four single microstrip patch antennas shown in Fig. 1, with $\lambda/2$ spacing, as shown in Fig. 4.

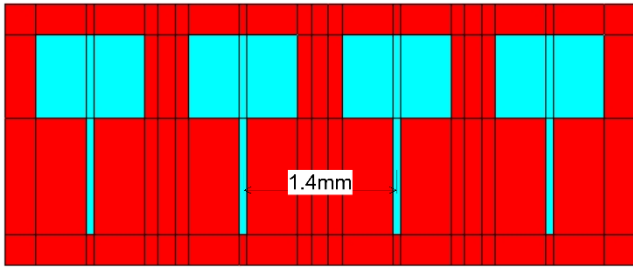


Fig. 4. Antenna Array with $\lambda/2$ spacing.

Since the array is symmetrical, only first two antennas (from left to right) are connected to generators, G1 and G2. The third and fourth antennas are symmetrical, so it is assumed that inner antennas have identical, but mirrored radiation pattern, as well as the outer antennas.

Fig. 5 shows that H-plane radiation patterns of both inner and outer antenna are deformed compared to the radiation pattern of a single antenna from Fig. 3 (where H-plane radiation pattern was symmetrical). Inner antenna deformation is less significant because it is surrounded by identical antennas from both left and right side.

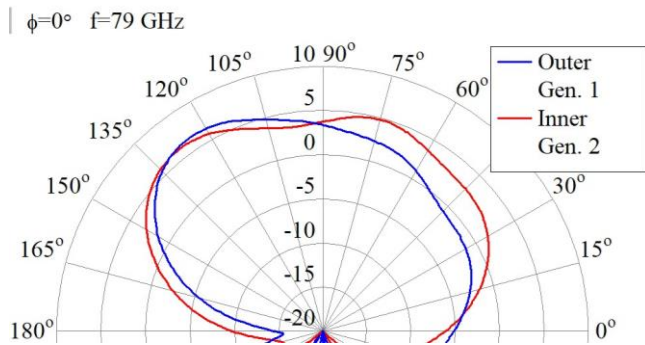


Fig. 5. Inner and Outer Antenna Radiation Patterns in H-plane.

IV. ANTENNA ARRAY WITH RADOME

Antenna array with a spherical radome of radius $d_{opt} + t = 13.42$ mm, with the center in the center of the array, is shown in Fig. 6.

Antenna array with a rectangular radome, with the same distance from the antenna array, having square cross section with the same width as the sphere radome diameter is shown in Fig. 7.

Both radomes are made from the material with relative permittivity 2 and thickness $t_{opt} = 2.68$ mm.

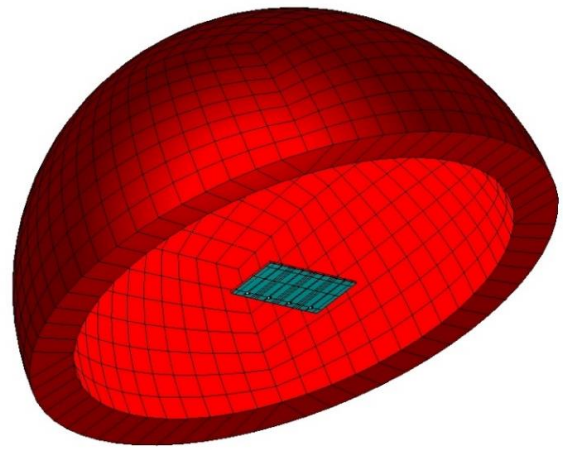


Fig. 6. Antenna array with the spherical radome.

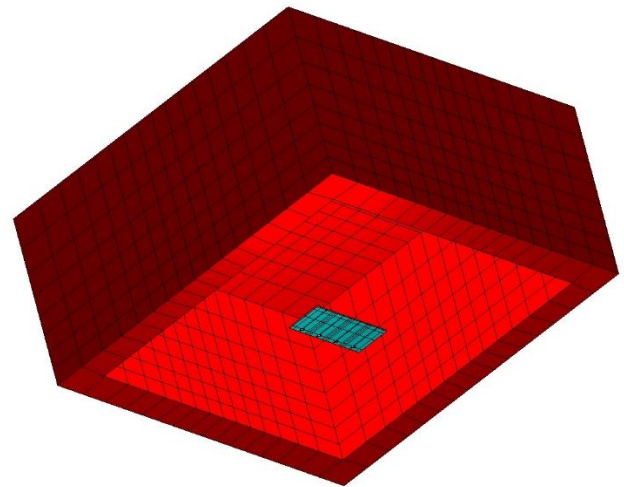


Fig. 7. Antenna array with the rectangular radome.

The electrical distance through the radome in boresight is equivalent to the thickness of the radome wall. The radome wall thickness t_{opt} is designed to cancel reflections from the radome, but in the case of normal incidence of the electromagnetic plane wave on infinite flat boundary. Therefore, at boresight of the radome, the reflections at the inner wall will mainly cancel, resulting in low net reflections.

In the case of a rectangular (flat) radome, when moving away from the boresight to higher grazing angles of arrival, the distance traveled by the mmWave signal is greater than “optimal thickness”, as illustrated in Fig. 8. This causes multiple reflections at the radome interface boundary resulting in ripples in the antenna radiation patterns and leading to nulls. These ripples and nulls can cause inconsistency in the detection of the objects at higher grazing angles resulting in angle estimation errors.

In the case of the spherical radome, the radome performance at different grazing angles will be more similar to the performance at boresight.

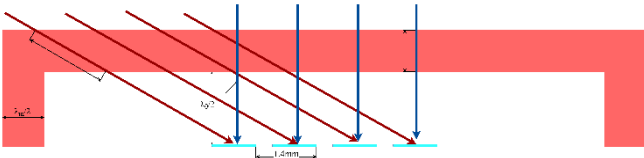


Fig. 8. Cross sectional view of the rectangular radome and the antenna array.

Radiation patterns of the outer antenna in E-plane, without a radome, and with spherical and rectangular radomes are shown in Fig. 9, whereas the similar graph for the inner antenna is shown in Fig. 10.

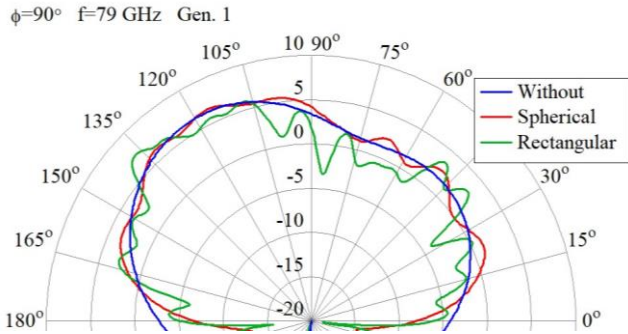


Fig. 9. Outer antenna radiation pattern in E-plane.

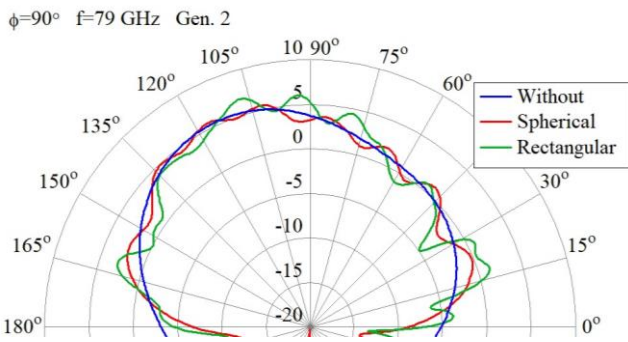


Fig. 10. Inner antenna radiation pattern in E-plane.

Radiation patterns of the outer antenna in H-plane, without a radome, and with spherical and rectangular radomes are shown in Fig. 11, whereas the similar graph for the inner antenna is shown in Fig. 12.

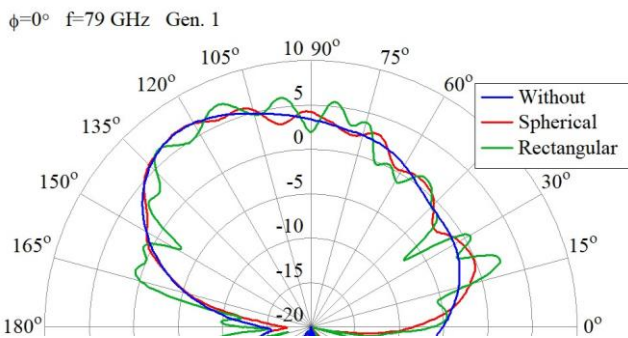


Fig. 11. Outer antenna radiation pattern in H-plane.

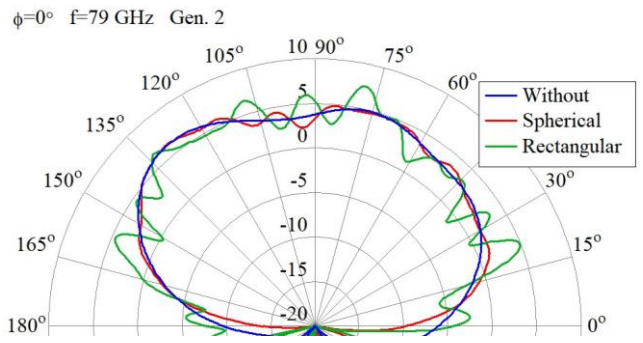


Fig. 12. Inner antenna radiation pattern in H-plane.

The radiation pattern from 180° to 360° is not interesting for the radar performance, also the simulation result is not relevant as the model doesn't include the complete PCB which is in reality much larger and has many components which are not modeled and neglected for the antenna simulation.

For the most applications azimuth angle of arrival estimation is more important. Therefore, the radiation patterns for H-plane (azimuth plane) are also shown in Cartesian system, in Figs. 13 and 14, to emphasize the ripples caused by radomes and to show the difference between the two radome shapes. Expected field of view of the automotive sensor is around ±60°, so antenna patterns from 15° to 165° are shown.

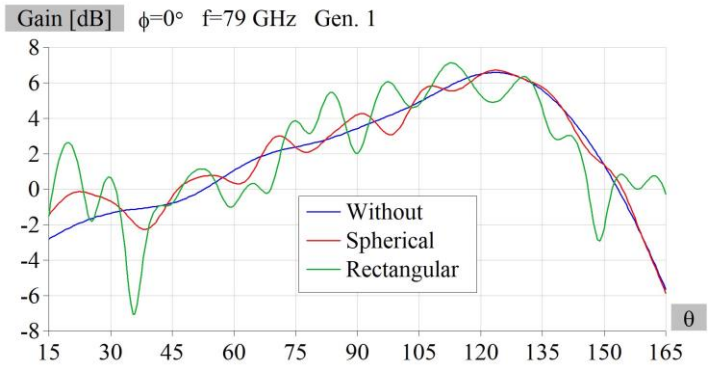


Fig. 13. Outer antenna radiation pattern in H-plane (Cartesian).

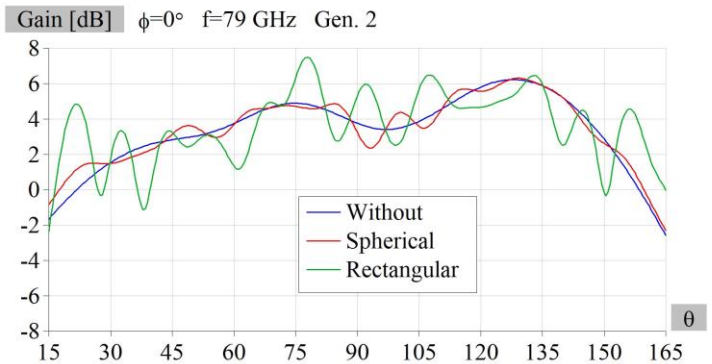


Fig. 14. Inner antenna radiation pattern in H-plane (Cartesian).

V. CONCLUSION

The aim of these simulations was to show whether the radome shape could improve automotive radar sensor performance and if it makes sense to invest in designing more complicated radome shapes compared to the most common rectangular design. The simplified model comprising of only 4 Rx antennas (typically mmWave sensors are using 4 Rx and 3 Tx antennas) is showing that spherical radome has significantly reduced ripples compared to the flat radome.

Also, the spherical radome cannot fulfill half wavelength conditions for each antenna, so some of the ripples still appear comparing to the scenario without a radome.

Main influence of the above-mentioned ripples is the degradation of the radar performance by means of angle of arrival estimation and the maximal detection range. To confirm the simulation results, a realistic antenna array with both Rx and Tx antennas should be measured using Vector Network analyzer (VNA) and referent (horn) antenna using different radomes. Also, the complete mmWave sensor with the identical antenna array and targets at different angle of

arrival could be tested to indicate the angle estimation accuracy degradation introduced by different radomes and compared with the radar simulation results.

REFERENCES

- [1] K. M. Strohm, H. L. Bloecher, R. Schneider and J. Wenger, "Development of future short range radar technology," *European Radar Conference, 2005. EURAD 2005.*, 2005, pp. 165-168.
- [2] M. M. S. Hossain *et al.*, "Wideband Radomes for Millimeter-Wave Automotive Radars," in *IEEE Transactions on Antennas and Propagation*, vol. 70, no. 2, pp. 1178-1186, Feb. 2022.
- [3] S. Buitrago, S. Blanch and J. Romeu, "Automotive radar and radome calibration to improve the direction of arrival detection performance," *12th European Conference on Antennas and Propagation (EuCAP 2018)*, 2018, pp. 1-5.
- [4] F. Fitzek and R. H. Rasshofer, "Automotive Radome Design - Reflection Reduction of Stratified Media," in *IEEE Antennas and Wireless Propagation Letters*, vol. 8, pp. 1076-1079, 2009.
- [5] C. K., H. U. R. M. and G. P. Authors, "mmWave Radar Radome Design Guide," TI, Dallas, Texas, USA, 2021.
- [6] A. Đorđević, *Elektromagnetika*, Akademska misao, Beograd, 2008.
- [7] A. Pandey, *Practical Microstrip and Printed Antenna Design*, Artech House, 2019.
- [8] <https://wipl-d.com/products/wipl-d-pro/>.

Implementing Gradient Model for Surface Roughness in WIPL-D

Milan P. Radović, Aleksandar Z. Golubović *Student Member, IEEE* and Miloš M. Jovičić

Abstract—The implementation of gradient method for surface roughness correction in WIPL-D software package is presented. Surface roughness model is tested on modified ring resonator model. Finally, simulation results from WIPL-D and CST Studio Suite are compared.

Index Terms—surface roughness, gradient model, effective conductivity, WIPL-D, ring resonator, surface impedance

I. INTRODUCTION

MODERN automotive radar systems are often developed in mm-Wave technology [1],[2] and require precise design and manufacturing. Hence, accurate full-wave electromagnetic modeling of such systems has an immense importance in development. To that aim, many electromagnetic effects, that are negligible at lower frequencies, should be taken into consideration at higher frequencies. One of such effects is surface roughness of conductors.

In this case study, gradient method [3] for surface roughness approximation is implemented in WIPL-D software package [4]. The implementation is tested on a model of modified ring resonator [5]. The results are then compared to the results acquired by CST Studio Suite [6].

Skin effect is a tendency of alternating currents to concentrate on the surfaces of conductors, and exponentially drop with conductor depth. It is a result of opposing Eddy currents induced by the changing magnetic fields. If a cylindrical wire-like conductor is observed, the countering Eddy currents will be strongest along the center of the cylinder and drop towards the surface. This will create a characteristic current density profile in the conductor, as shown in Fig. 1. With higher frequencies, currents are more concentrated at the surface of the conductor. We define skin depth, δ , as the depth at which the current density drops to $\frac{1}{e}$ of its value (around 36.7%)

Skin depth is given by [7]

$$\delta = \sqrt{\frac{2\rho}{\omega\mu}} \sqrt{\sqrt{1 + (\rho\omega\varepsilon)^2} + \rho\omega\varepsilon}, \quad (1)$$

Milan P. Radović is with the School of Electrical Engineering, University of Belgrade, 73 Bulevar kralja Aleksandra, 11020 Belgrade, Serbia and with NOVELIC d.o.o., Veljka Dugosevica 54/B5, 11000 Belgrade, Serbia (e-mail: milan.radovic@novelic.com).

Aleksandar Z. Golubović is with the School of Electrical Engineering, University of Belgrade and with NOVELIC d.o.o. (e-mail: aleksandar.golubovic@novelic.com).

Miloš M. Jovičić is with NOVELIC d.o.o. (e-mail: milos.jovicic@novelic.com)

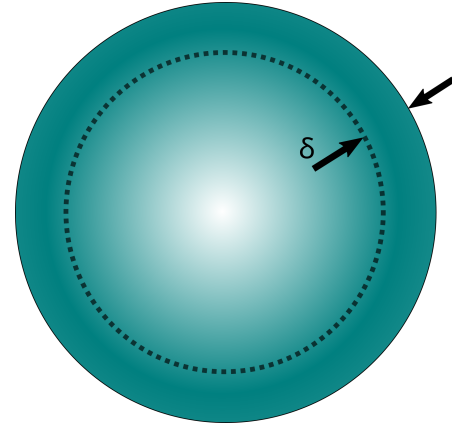


Fig. 1: Illustration of current density and the skin depth.

where ρ is the specific electrical resistance, ω is the angular frequency of current, μ is the permeability of the conductor and ε permittivity. At frequencies of interest, (1) can be approximated by

$$\delta = \sqrt{\frac{2}{\sigma\omega\mu}}. \quad (2)$$

At low frequencies, the skin depth is larger than the imperfections of the conductor surface. Therefore, when modeling conductors for electromagnetic analysis it is common to approximate the surface of the conductor as ideally flat. However, at high frequencies the skin depth is small enough that it is of comparable size to the roughness of the surface (0.23 μm at 80 GHz). The rough surface of the conductor and the comparable skin depth qualitatively make the current paths longer. At microscopic levels, the roughness structures are electrically larger causing resonant frequencies to shift lower. Additionally, longer current paths will induce larger resistive losses.

We define R_q as the root mean square average of the profile height deviations from the mean line of ideal surface. Different copper deposition methods will yield different surface profiles with different R_q . Some of the most widely used copper profiles are [8] STD (Standard foil, $R_q = 5 - 10 \mu\text{m}$), HPF (High Performance Foil, $R_q = 10 - 15 \mu\text{m}$), RTF (Reverse Treated Foil, $R_q = 3 - 6 \mu\text{m}$), VLP (Very Low Profile, $R_q = 3 - 6 \mu\text{m}$), HVLP (Hyper Very Low Profile, $R_q = 1 - 3 \mu\text{m}$) and ULP (Ultra Low Profile, $R_q = 0.5 - 1 \mu\text{m}$), which are shown in Fig. 2. At 1 GHz, the skin depth is 2 μm and is considerably smaller than most copper profile R_q . Since

most of the high frequency current will be conducted through irregular boundary surface, it is important to realistically model and correct for the effects which the rough surface will induce.

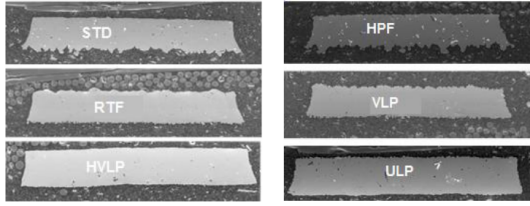


Fig. 2: Microscopic images of common copper deposition profiles.

II. GRADIENT METHOD

The gradient method relies on the fact that the surface profile can be described as a conductivity gradient, from conducting copper to non-conductive dielectric.

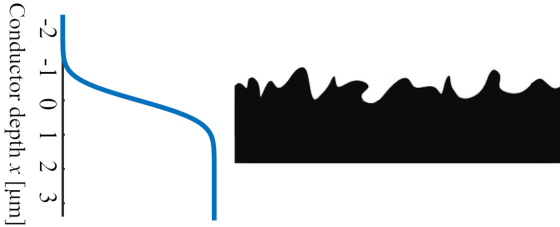


Fig. 3: An example of conductor surface profile and its cumulative distribution function.

It is evident from [3] that the conductivity, $\sigma(x)$, is a cumulative distribution function of x

$$\sigma(x) \propto CDF(x). \quad (3)$$

Cumulative distribution function is given as the integral of probability distribution function over the entire x domain

$$CDF(x) = \int_{-\infty}^x PDF(u) du. \quad (4)$$

We approximate the probability distribution function with a normal Gauss distribution

$$PDF(x) = \frac{1}{R_q \sqrt{2\pi}} e^{-\frac{x^2}{2R_q^2}}. \quad (5)$$

Finally, the conductivity function can be written as

$$\sigma = \sigma_0 CDF(x) = \sigma_0 \int_{-\infty}^x \frac{1}{R_q \sqrt{2\pi}} e^{-\frac{u^2}{2R_q^2}} du. \quad (6)$$

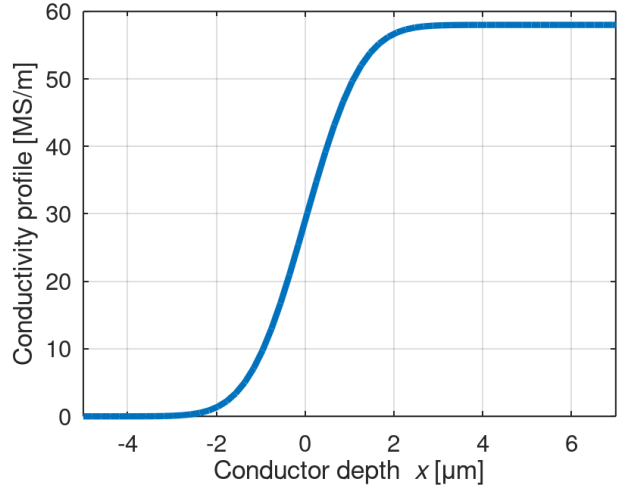


Fig. 4: Conductivity profile of copper surface for $R_q = 1 \mu\text{m}$.

Next, wave equations are derived with additional term that corresponds to variable conductivity due to surface roughness [3]

$$\frac{\partial^2 B_y}{\partial x^2} - j\omega\mu_0\sigma B_y - \frac{\partial}{\partial x} \ln(\sigma(x)) \frac{\partial B_y}{\partial x} = 0, \quad (7)$$

where B is magnetic flux density vector. It should be noted that when the conductivity profile is constant, (7) simplifies down to classical Helmholtz equation which is analytically solvable. However, (7) needs to be numerically solved.

Finite differences method is used to solve (7) for B_y . The results are presented in Fig. 5.

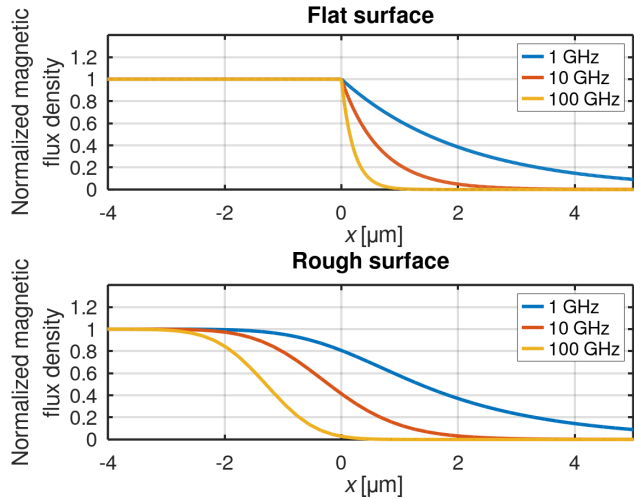


Fig. 5: Comparison of magnetic flux density y component for flat and rough surface ($R_q = 1 \mu\text{m}$).

The change in magnetic flux density is gradual and not sharp as in the flat approximation, which is more in accordance to the real scenario. Knowing the magnetic flux density it is possible to find the current density distribution given by Fig. 6

$$J_z = \frac{1}{\mu_0} \frac{\partial B_y}{\partial x}. \quad (8)$$

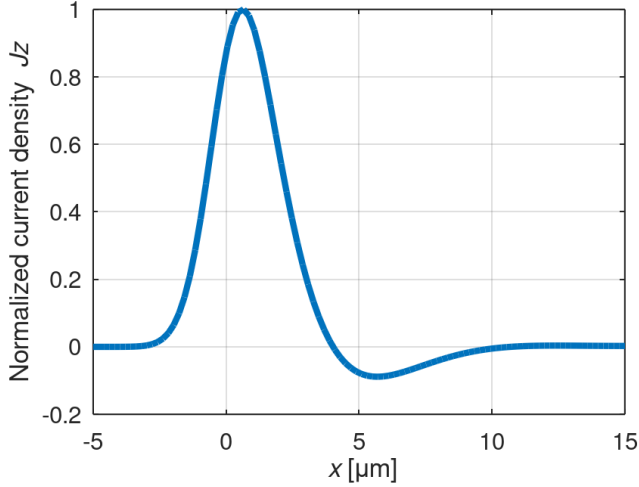


Fig. 6: Normalized current density distribution.

III. EFFECTIVE CONDUCTIVITY

The power density of the conductor surface is given by [3]

$$P_d = \int_{\sigma>0} \frac{|J|^2}{2\sigma(x)} dx. \quad (9)$$

Consider another conductor with a flat surface that has the same power density as observed rough surface conductor. Its conductivity profile will be a step function

$$\sigma(x) = \begin{cases} \sigma_{\text{eff}}, & x < 0 \\ 0, & x > 0 \end{cases}. \quad (10)$$

By equalizing the two power distributions, we can calculate the effective conductivity that a flat conductor will need to have, in order to reproduce the same power distribution as a rough surfaced one

$$\int_{\sigma>0} \frac{|J_{\text{rough}}|^2}{2\sigma(x)} dx = \int_{\sigma>0} \frac{|J_{\text{flat}}|^2}{2\sigma_{\text{eff}}} dx. \quad (11)$$

Finally, effective conductivity for different R_q values is numerically computed (7).

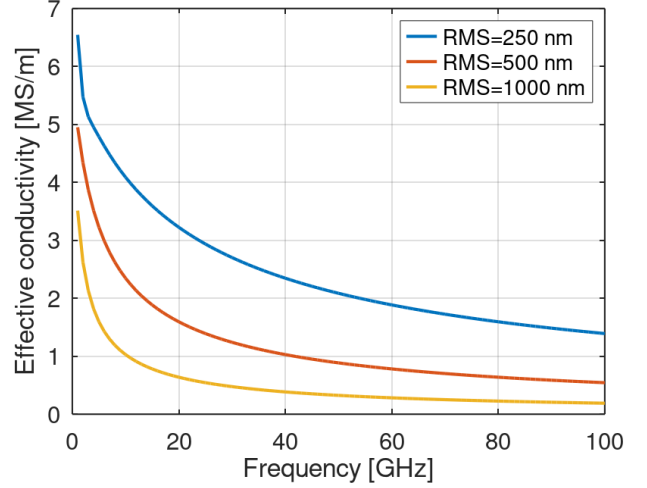


Fig. 7: Comparison of effective conductivity in function of frequency for different values of R_q .

IV. EFFECTIVE PERMEABILITY

Previous method models the resistive losses that will be induced from the surface roughness, however, due to different surface profile the conductor will have different reactive losses.

Similarly to previous modeling of effective conductivity, we will model an effective permeability to account for reactive losses. We observe another conductor with identical magnetic field energy distribution, however, with effective permeability. Equalizing the two energy distributions we can calculate the effective permeability as

$$\int_{\sigma>0} \frac{|B_{y,\text{rough}}|^2}{2\mu_0\mu_r} dx = \int_{\sigma>0} \frac{|B_{y,\text{flat}}|^2}{2\mu_0\mu_{r,\text{eff}}} dx. \quad (12)$$

By numerically solving, we yield (Fig. 8):

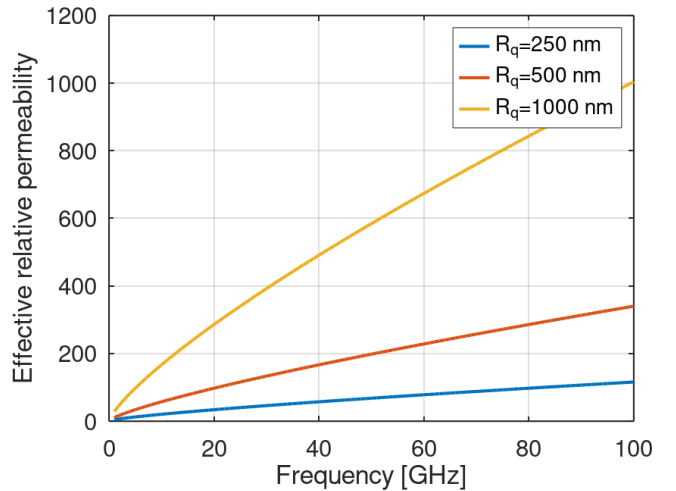


Fig. 8: Comparison of effective permeability in function of frequency for different values of R_q .

V. IMPLEMENTATION AND RESULTS

By obtaining both conductivity and permeability, we can model both resistive and reactive losses. The software package WIPL-D can model distributed loadings with surface impedance, hence we need to translate our parameters into surface impedance as,

$$Z_s = R_s + jX_s = \frac{1}{\sigma_{\text{eff}}\delta(\sigma_{\text{eff}})} + \frac{1}{\sigma_0\delta(\mu_{r,\text{eff}})}. \quad (13)$$

We model a modified ring resonator in both WIPL-D and CST Studio Suite for the purposes of result comparison (Figure 9). In CST we use the surface roughness method provided with the software, while in WIPL-D we use the frequency table function to implement the surface impedance into the model.

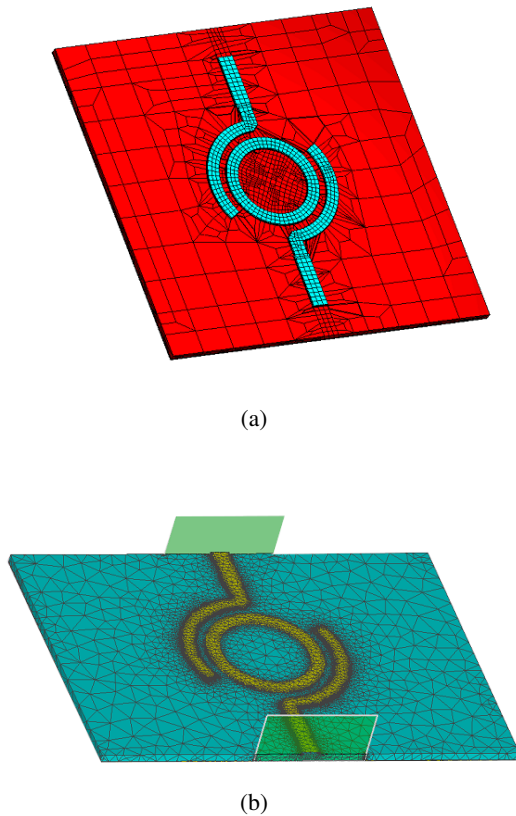


Fig. 9: a) Ring resonator model in WIPL-D and b) ring resonator model in CST

Since CST uses gradient method that accurately model surface roughness, matching of results obtained by CST and WIPL-D will prove a successful implementation of gradient method in WIPL-D.

The comparison of simulated reflection coefficient for both flat and rough surface of modified ring resonator is shown in 10. From these figures we can observe that there is an excellent matching between the results, thus the gradient method is successfully implemented in WIPL-D.

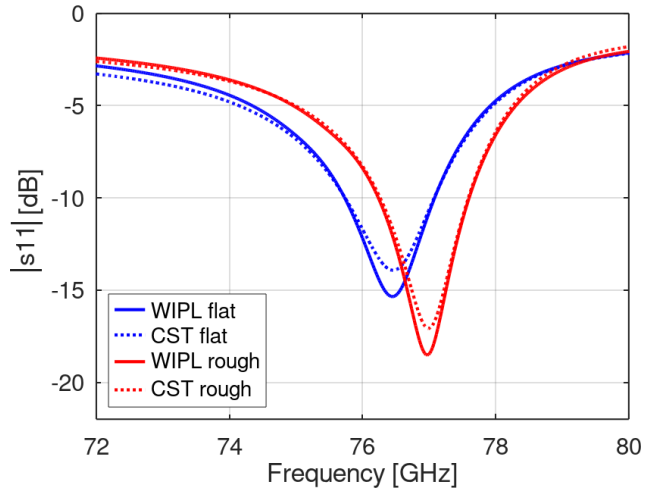


Fig. 10: Comparison of s_{11} for CST and WIPL-D.

VI. CONCLUSION

Gradient method for surface roughness estimation is implemented in WIPL-D and tested on modified ring resonator model. Results match the ones obtained using CST Studio Suite, thus gradient model implementation is corroborated. This method can be utilized in WIPL-D, for mm-Wave designs, where surface roughness is crucial.

REFERENCES

- [1] Baolong Jian, Jing Yuan, and Qiqin Liu. "Procedure to Design a Series-fed Microstrip Patch Antenna Array for 77 GHz Automotive Radar". In: *2019 Cross Strait Quad-Regional Radio Science and Wireless Technology Conference (CSQRWC)*. 2019, pp. 1–2.
- [2] Sungjun Yoo et al. "Patch Array Antenna Using a Dual Coupled Feeding Structure for 79 GHz Automotive Radar Applications". In: *IEEE Antennas and Wireless Propagation Letters* 19.4 (2020), pp. 676–679.
- [3] Gerald Gold and Klaus Helmreich. "A Physical Surface Roughness Model and Its Applications". In: *IEEE Transactions on Microwave Theory and Techniques* 65.10 (2017), pp. 3720–3732.
- [4] WIPL-D. <https://wipl-d.com>.
- [5] Piotr Jankowski-Mihułowicz et al. "Determination of the Material Relative Permittivity in the UHF Band by Using T and Modified Ring Resonators". In: *International Journal of Electronics and Telecommunications* 62 (June 2016).
- [6] CST Studio Suite. <https://www.3ds.com/products-services/simulia/products/cst-studio-suite>.
- [7] Vander Vorst Andre; Rosen Arye; Kotsuka Youji. *RF/Microwave Interaction with Biological Tissues*. Wiley-Interscience, p. 41.
- [8] Aleksei V. Rakov et al. "Quantification of Conductor Surface Roughness Profiles in Printed Circuit Boards". In: *IEEE Transactions on Electromagnetic Compatibility* 57.2 (2015), pp. 264–273.

The Ability to Minimize a New Type of Moderate-Bandwidth Microwave Filter

Dušan Nešić, *Member, IEEE*, Tomislav Milošević

Abstract—An example of minimizing the width of a microwave filter structure by bending the stubs and reducing the number of required via holes is presented in this paper. It is shown that the filter area can be reduced near 2 times after bending the stubs. EM model of minimized structure is presented and compared with common filter design.

Index Terms—Microwave filter, Minimization, Microstrip.

I. INTRODUCTION

WIDE bandpass filters (WBPFs) are important components found in microwave circuits [1-8]. Their purpose is to suppress DC components of the signal as well as low frequency signal components. This suppression is achieved by combing coupling and short-circuiting stubs [1-4] or by only short-circuiting stubs [5-8]. Also, the defective ground structure (DGS) or multilayers can be also used with the same purpose [1,4].

Fig. 1 shows an infinite periodical series of identical T-cells with a short-circuited stub and uniform lines implemented in microstrip technology. Here, Z and Z_s represent characteristic impedances of the base line θ and stub θ_s . θ is electrical length given as the phase for a given frequency or wavelength ($\theta=2\pi L/\lambda$). Central passband frequency f_c corresponds to $\theta_s = \pi/2$ i.e., $L = \lambda_c/4$. λ_c is wavelength for the frequency f_c .

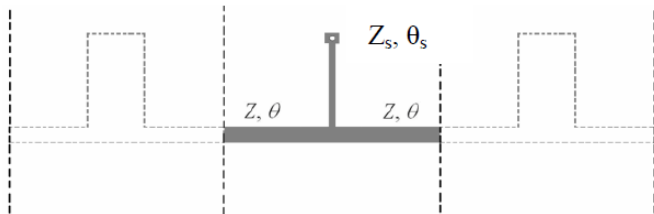


Fig. 1. Scheme of one cell within a filter in microstrip technology.

In [9, 10] relation $\theta_s = 2\theta$ was chosen to eliminate ripples in the stopband. For that relation optimized S_{11} -parameters are for $Z = 50 \Omega$ for all values of Z_s . Calculated design curve of Z_s on the relative bandwidth (RBW) is presented in Fig. 2.

The film for fabrication (etching) for 4-cells filter with the dimensions is outlined in Fig. 3 [10]. Central frequency is 3 GHz while used substrate is FR-4 with $\epsilon_r = 4.3$. RBW is

100% (1.00) for $Z_s = 60.5$ Ohms. The dimensions of the metallization (black surfaces in the Fig. 3) are $15 \mu\text{m}$ (0.015 mm) wider on both sides ($2 \times 15 \mu\text{m}$) in order to compensate the lateral etching.

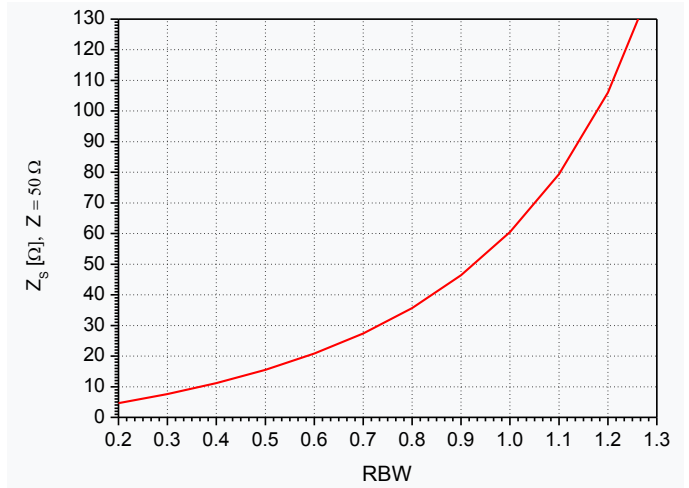


Fig. 2. Design curve of Z_s depending on RBW for $Z = 50 \Omega$ [9, 10].

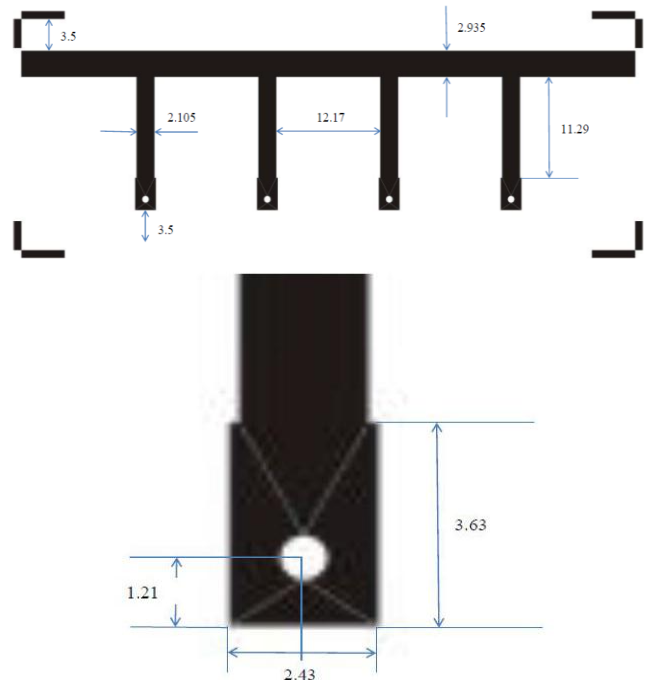


Fig. 3. Dimensions of the film used for etching in mm. Hole radius is equal to 0.385 mm (0.4 mm – 0.015 mm) [10].

Dušan Nešić is with Centre of Microelectronic Technologies, Institute of Chemistry, Technology and Metallurgy, University of Belgrade, Njegoševa 12, 11000 Belgrade, Serbia (e-mail: nesicad@nanosys.ihtm.bg.ac.rs).

Tomislav Milošević is with WIPL-D d.o.o., Gandijeva 7, 11073 Belgrade, Serbia (e-mail: tomislav.milosevic@wipl-d.com)

One of the problems with all structures, including filters, is minimization. Here, one cell has an area of about $\lambda_c^2/16$ (λ_c is wavelength for the central passband frequency f_c). The area can be reduced by bending the stubs and connecting the pair of stubs to one via [8].

II. MINIMIZATION

Bending the stubs and connecting a pair of stubs to one via is possible according to the relation $\theta_s = 2\theta$. Actually, the length of one stub is approximately the same as the length of a line between the stubs, see Fig. 3. The EM model of the commonly used filter (the model without bending stubs) and the model of the filter with bent stubs are all presented in the Fig. 4 in Program Package WIPL-D [11]. After bending, the area of the filter is reduced near 2 times. The comparison of calculated S-parameters is given in the Fig. 5. A good agreement between the results can be noted.

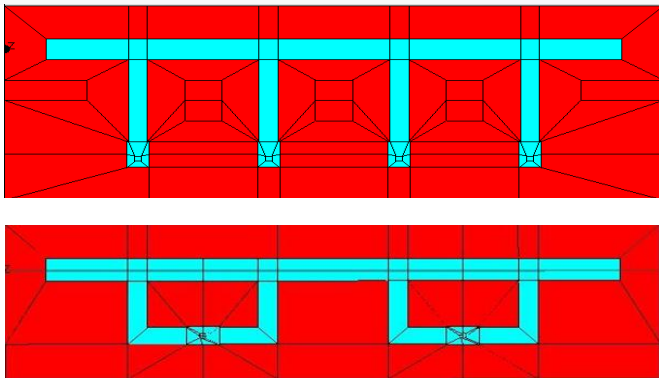


Fig. 4. Commonly used model and the model with bending of the stubs.

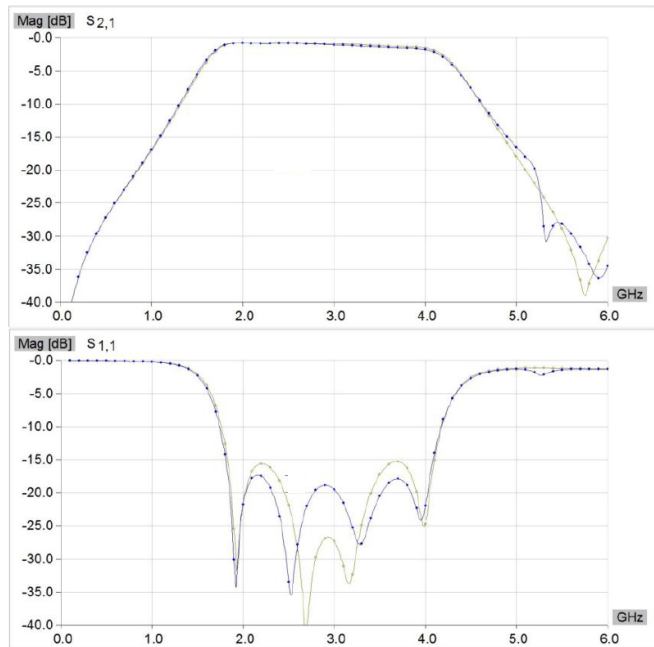


Fig. 5. The comparison between the S-parameters of the commonly used model and the model with bent stubs which are displayed in Fig. 4. No bending (yellow); Bending (blue).

The solution with low Z_s values, i.e. implementation with wide microstrip stubs, can be realized as a parallel connection of branches with two times higher Z_s . The EM model for 2 times lower Z_s than the model presented in Fig. 4 ($Z_s = 60.5 \Omega / 2 = 30.25 \Omega$) is outlined in Fig. 6 in Program Package WIPL-D [11]. That way the filter achieves relative bandwidth of about 75% (0.75) according to Fig. 2. It is accompanied by the model with bending stubs.

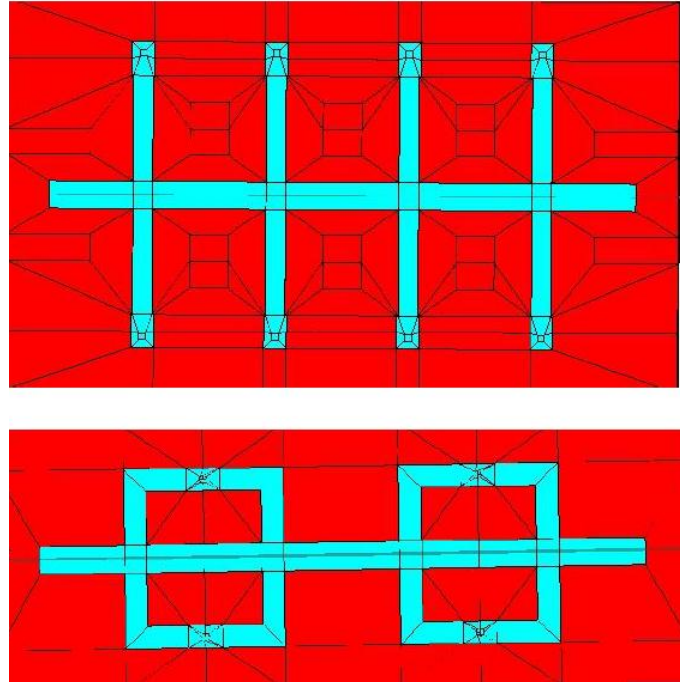


Fig. 6. EM model of the filter with parallel connection of stubs with twice higher Z_s and the model with bent stubs.

The comparison between the S-parameters of the model without and the model with bending is shown in Fig. 7. It can be seen that, if the parameter S_{21} is observed, the model with stub bending gives a bit “worse”, but still acceptable result in the higher frequency stop-band. The filter area is also reduced near 2 times.

III. CONCLUSION

An example of minimizing the width of the filter structure by bending the branches as well as reducing the number of required holes for vias was presented. A solution applying low impedances, i.e., wide microstrip lines of branches, was also given, as a parallel connection of branches with twice as large Z_s . It is accompanied with a model with bending of branches and minimization.

It can be seen that minimization of the filters was performed successfully and that responses of the filters after bending the stubs are almost the same as the response of the commonly designed filters.

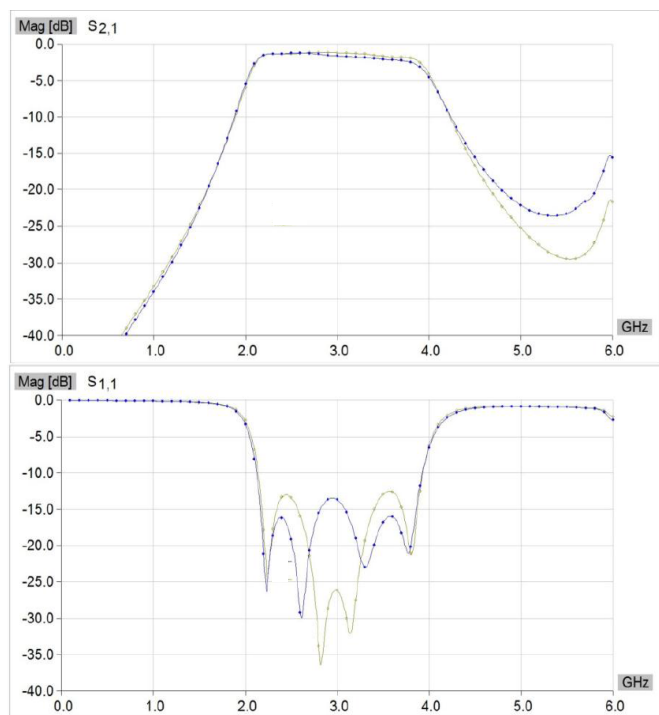


Fig. 7. The comparison of the S-parameters of the model without and with bending in Fig. 6. No bending (yellow); Bending (blue).

ACKNOWLEDGMENT

This work was financially supported by Ministry of Education, Science and Technological Development of the Republic of Serbia (Grant No. 451-03-68/2022-14/200026).

REFERENCES

- [1] Z.-C. Hao and J.-S. Hong, "Ultrawideband filter technologies," *IEEE Microwave Magazine*, vol.11, no.4, pp.56-68, 2010.
- [2] R. Zhang and D. Peroulis, "Planar Multifrequency Wideband Bandpass Filters With Constant and Frequency Mappings," *IEEE Transactions on Microwave Theory and Techniques*, vol.66, no.2, pp.935-942, 2018.
- [3] R. Zhang, S. Luo, L. Zhu, "A New Synthesis and Design Method for Wideband Bandpass Filters with Generalized Unit Elements," *IEEE Transactions on Microwave Theory and Techniques*, vol. 65, no. 3, pp. 815-823, 2017.
- [4] L.-T. Wang, Y. Xiong and M. He (2019), "Review on UWB Bandpass Filters, UWB Technology - Circuits and Systems," Mohamed Kheir, Intech Open, DOI: 10.5772/intechopen.87204. Available from: <https://www.intechopen.com/books/uwb-technology-circuits-and-systems/review-on-uwb-bandpass-filters>.
- [5] M. S. Razalli, A. Ismail, M. A. Mahd and M. N. Hamidon, "Compnact Configuration Ultra- Wideband Microwave Filter Using Quarter-Wave Length Short-Circuited Stub," *Proceedings of Asia-Pacific Microwave Conference 2007*.
- [6] J.-S. Hong and H. Shaman, "An Optimum Ultra-Wideband Microstrip Filter," *Microwave and Optical Technology Letters*, vol. 47, no. 3, pp.230-233, 2005.
- [7] M. S. Razalli A. Ismail, M. A. Mahdi and M. N. Hamidon, "Ultra-Wide Band Microwave Filter Utilizing Quarter-wavelength Short-Circuited Stubs," *Microwave and Optical Technology Letters*, Vol. 50, no. 11, pp. 2981-2983, 2008.
- [8] M. S. Razalli, A. Ismail, M. A. Mahdi and M. N. Hamidon, "Compact Ultra-Wide Band Microwave Filter Utilizing Quarter-Wave Length Short Circuited Stubs with Reduced Number of Vias," *Microwave and Optical Technology Letters*, vol. 51, no. 9, pp. 2116-2119, 2009.
- [9] D. A. Nestic, One new solution of algorithm for wide bandpass filters, 2020 28th Telecommunications Forum, TELFOR 2020 – Proceedings
- [10] D. Nestic, and T. Milosevic, Application of a New Algorithm for the Wide Bandpass Filters, TELSISKS 2021
- [11] *Program Package WIPL-D Pro v18 (WIPL-D d.o.o, Belgrade 2022. www.wipl-d.com)*

Uopštenje izraza za transfer funkcije između antena u problemima inverznog rasejanja

Anja Kovačević, Marija Nikolić Stevanović, *Member, IEEE*, i Antonije Đorđević

Apstrakt—U radu su izvedeni izrazi za priraštaje koeficijentata rasejanja proizvoljnog para antena usled prisustva rasejača koji se nalazi u linearnoj nehomogenoj sredini. Glavni doprinos rada je uopštenje izraza za slučaj kada sredina u kojoj se nalazi rasejač poseduje magnetska svojstva. Takođe je pokazano da dobijeni izraz važi i u slučaju kada su nominalne impedanse pristupa različite i kompleksne.

Cljučne reči—Mikrotalasno formiranje slike; antenska merenja; transfer funkcija.

I. UVOD

Mikrotalasi imaju brojne primene u određivanju lokacije ili oblika nedostupnih objekata, poput detekcije zakopanih objekata pomoću radara za podzemna ispitivanja [1], pozicioniranja objekata iza zidova [2], medicinske dijagnostike [3] i nedestruktivnog ispitivanja materijala [4]. Svim navedenim aplikacijama zajedničko je korišćenje antena koje emituju elektromagnetsko zračenje, a potom mere perturbaciju elektromagnetskog polja usled prisustva ispitivanog objekta (rasejano polje). Većina algoritama za dobijanje slike polazi od jednačine inverznog rasejanja koja povezuje rasejano električno polje i izvore polja, odnosno indukovane struje u objektu [5]. Međutim, izlazi mernih sistema nisu vektorske veličine poput rasejanog električnog polja. Umesto toga, rezultati merenja [6] su najčešće skalarne veličine poput s -parametara [7]. Zbog toga je neophodno transformisati jednačinu rasejanja tako da u njoj figurišu veličine koje se zaista dobijaju kao rezultat eksperimenta. Izraz za bistatički prenos između realnih antena prvi put je izveden u [8], za slučaj kada se antene nalaze u vakuumu. Izvođenje je generalizovano u [9] tako da važi za proizvoljnu linearnu nemagnetsku sredinu. U [10] je prikazano alternativno izvođenje izraza za bistatički prenos na osnovu teoreme reciprociteta za elektromagnetska polja [11], [12]. U ovom radu se produbljuju izvođenja iz [10] tako što i rasejač, i okolna sredina mogu biti proizvoljni linearni dielektrici (tj. mogu posedovati magnetska svojstva). Takođe, uopštava se merni sistem tako što se dopušta da pristupi antena imaju različite nominalne impedanse, koje mogu biti kompleksne veličine.

Rad je organizovan na sledeći način. Nakon opštih razmatranja u Uvodu, u drugom poglavlju je izveden izraz za napon praznog hoda na pristupu prijemne antene usled prisustva rasejača, odakle se dobijaju izrazi za priraštaje impedansnih parametara. Zatim je izveden izraz za priraštaj napona na prilagođenom prijemniku, odakle su, zajedno sa Penfield-Kurokawa relacijama [7], određeni priraštaji parametara rasejanja između antena usled prisustva rasejača.

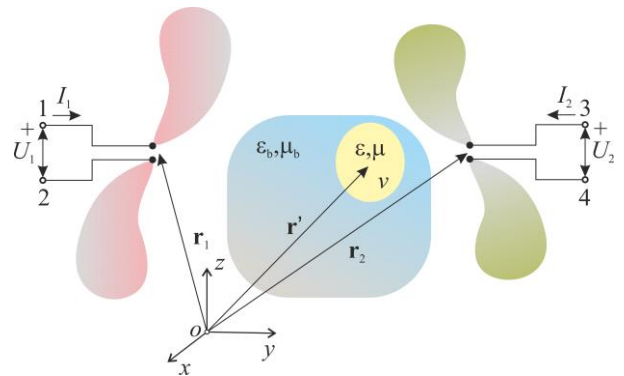
A. Kovačević, M. Nikolić Stevanović, i A. Đorđević – Univerzitet u Beogradu – Elektrotehnički fakultet, Bulevar kralja Aleksandra 73, 11020 Beograd, Srbija (e-mail: ka180112d@student.etf.bg.ac.rs, mnikolic@etf.rs, edjordja@etf.bg.ac.rs).

II. ELEKTROMAGNETSKI MODEL

A. Priraštaji impedansnih parametara

Posmatramo mikrotalasni merni sistem, namenjen za dobijanje slike nedostupnih objekata u kome, radi jednostavnosti, postoje samo dve antene (slika 1). Nedostupni objekat je na slici označen žutom bojom i nalazi se u linearnoj nehomogenoj sredini, koju nazivamo okolni medijum. U opštem slučaju okolni medijum obuhvata dielektrik (obojen plavom bojom) koji sakriva objekat, medijum u kome se nalaze antene, kao i metalne i dielektrične delove antena.

Sva izvođenja koja slede, važe i za merni sistem koga čini proizvoljan broj antena.



Slika 1. Merna postavka sa definisanim referentnim smerovima struja i napona na pristupima antena.

Merni sistem možemo da posmatramo kao dvoportnu mrežu opisanu impedansnim (z) parametrima ili parametrima rasejanja (s) [7]. Pretpostavićemo da leva (prva) antena radi kao predajna, a desna (druga) kao prijemna. Predajna antena napaja se idealnim strujnim generatorom struje I_1 , a priključci prijemne antene su otvoreni ($I_2 = 0$). Na slici 1 su prikazani usvojeni referentni smerovi za struje i napone na priključcima antena. Međusobna impedansa, z_{21} , definiše se kao

$$z_{21} = \left. \frac{U_2}{I_1} \right|_{I_2=0}, \quad (1)$$

gde je U_2 napon praznog hoda prijemne antene. U problemima inverznog rasejanja koristi se i priraštaj međusobne impedanse, koji se definiše kao

$$\Delta z_{21} = \frac{\Delta U_{2,o.c.}}{I_1} = \frac{U_{2,o.c.} - U_{2,o.c.}^0}{I_1}, \quad (2)$$

gde su $U_{2,oc}$ i $U_{2,oc}^0$ naponi praznog hoda indukovani na pristupima antene u prisustvu i odsustvu rasejača, a $\Delta U_{2,oc}$ njihova razlika. Usvajajući oznake sa slike 1, imamo da je

$$\Delta U_{2,oc} = \int_3^4 (\mathbf{E}_{tot}^1 - \mathbf{E}_{inc}^1) \cdot d\mathbf{l} = \int_3^4 \mathbf{E}_s^1 \cdot d\mathbf{l}, \quad (3)$$

gde je \mathbf{E}_{tot}^1 vektor ukupnog električnog polja (polje u prisustvu rasejača), \mathbf{E}_{inc}^1 vektor incidentnog električnog polja (polje u odsustvu rasejača), a \mathbf{E}_s^1 vektor rasejanog električnog polja, pri čemu gornji indeks označava predajnu antenu.

Prema zapreminskoj teoremi ekvivalencije, izvori rasejanog polja su ekvivalentne električne i magnetske struje koje se nalaze u okolnom medijumu [5], [6]. (Ti izvori zamenjuju rasejač.) Ekvivalentne struje postoje samo unutar zapremine rasejača, a njihove zapreminske gustine određene su vektorima

$$\mathbf{J}_{eq}^1(\mathbf{r}') = j\omega(\varepsilon - \varepsilon_b)\mathbf{E}_{tot}^1(\mathbf{r}'), \quad (4)$$

$$\mathbf{M}_{eq}^1(\mathbf{r}') = j\omega(\mu - \mu_b)\mathbf{H}_{tot}^1(\mathbf{r}'), \quad (5)$$

gde je \mathbf{r}' vektor položaja proizvoljne tačke u rasejaču, ε i μ su permitivnost i permeabilnost rasejača, ε_b i μ_b su permitivnost i permeabilnost okolnog medijuma, a $\mathbf{H}_{tot}^1(\mathbf{r}')$ je vektor ukupnog magnetskog polja u tački \mathbf{r}' (polje u prisustvu rasejača). Primena zapreminske teoreme ekvivalencije i odgovarajući naponi prikazani su na slici 2.

Da bismo odredili $\Delta U_{2,oc}$ primenićemo teoremu reciprociteta [11], [12] na scenario sa slike 2, u kome pobudu predstavljaju ekvivalentne struje ($\mathbf{J}_{eq}^1, \mathbf{M}_{eq}^1$), a odziv je rasejano polje na mestu prijemne antene (\mathbf{E}_s^1). Na slici 3 prikazan je obrnut scenario, u kome je prethodna pobuda ($\mathbf{J}_{eq}^1, \mathbf{M}_{eq}^1$) ukinuta, a na mestu tih struja je okolni medijum. Druga antena radi kao predajna i napaja se idealnim strujnim generatorom struje I_2 . S obzirom na to da je druga antena jedini izvor zračenja, kao i da nema rasejača, druga antena proizvodi incidentno električno i magnetsko polje ($\mathbf{E}_{inc}^2, \mathbf{H}_{inc}^2$). Gornji indeks sada označava predajnu antenu. Na osnovu teoreme reciprociteta važi

$$\int_v (\mathbf{E}_{inc}^2 \cdot \mathbf{J}_{eq}^1 - \mathbf{H}_{inc}^2 \cdot \mathbf{M}_{eq}^1) dv = \int_4^3 \mathbf{E}_s^1 \cdot I_2 d\mathbf{l} = -I_2 \Delta U_{2,oc}. \quad (6)$$

Iz (6) sledi

$$\Delta U_{2,oc} = -\frac{\int_v (\mathbf{E}_{inc}^2 \cdot \mathbf{J}_{eq}^1 - \mathbf{H}_{inc}^2 \cdot \mathbf{M}_{eq}^1) dv}{I_2}, \quad (7)$$

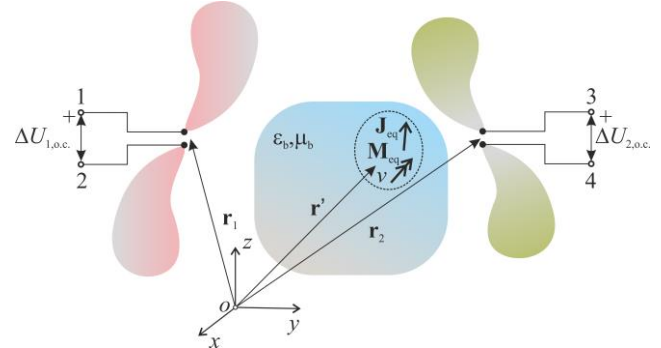
a iz (2) i (7) dobijamo

$$\Delta z_{21} = \frac{\Delta U_{2,oc}}{I_1} = -\frac{\int_v (\mathbf{E}_{inc}^2 \cdot \mathbf{J}_{eq}^1 - \mathbf{H}_{inc}^2 \cdot \mathbf{M}_{eq}^1) dv}{I_1 I_2}. \quad (8)$$

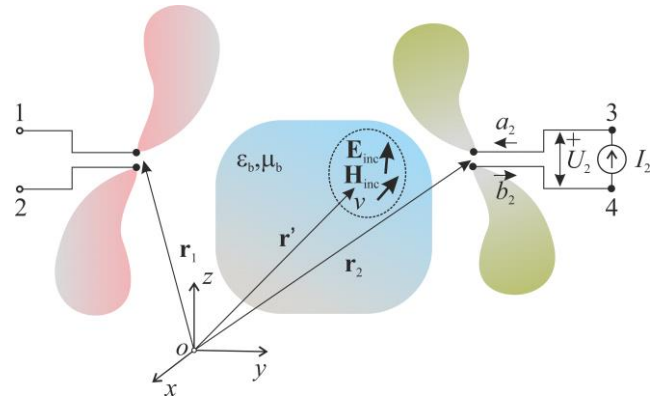
Isti postupak se može primeniti i kada niz čini M antena. U tom slučaju važi

$$\Delta z_{ji} = \frac{\Delta U_{j,oc}}{I_i} = -\frac{\int_v (\mathbf{E}_{inc}^j \cdot \mathbf{J}_{eq}^i - \mathbf{H}_{inc}^j \cdot \mathbf{M}_{eq}^i) dv}{I_j I_i}, \quad (9)$$

$i, j = 1, \dots, M.$



Slika 2. Ekvivalentne struje u okolnom medijumu kao izvori rasejanog polja i indukovanih napona na pristupima antena.



Slika 3. Primena teoreme reciprociteta za scenario ilustriran na slici 2.

B. Priraštaji parametara rasejanja

Slika 4 ilustruje pojednostavljenu mernu postavku koja je namenjena za određivanje s -parametara. Posmatramo opšti slučaj u kome su nominalne impedanse portova predajne i prijemne antene kompleksne veličine i iznose Z_{c1} i Z_{c2} , respektivno. Prva antena pobuđena je realnim naponskim generatorom unutrašnje impedanse Z_{c1} , a pristup druge antene zatvoren je impedansom Z_{c2} . Koeficijent transmisije definiše se kao

$$s_{21} = \frac{b_2}{a_1} \Big|_{a_2=0}, \quad (10)$$

gde je a_1 kompleksni intenzitet incidentnog talasa na pristupu prve antene, a b_2 kompleksni intenzitet reflektovanog talasa na pristupu druge antene. Penfield-Kurokawa izrazi za kompleksne intenzitete incidentnih i reflektovanih talasa („talasa snage“) [7] glase:

$$a_i = \frac{U_i + I_i Z_{ci}}{2\sqrt{R_{ci}}}, \quad (11)$$

$$b_i = \frac{U_i - I_i Z_{ci}^*}{2\sqrt{R_{ci}}}, \quad (12)$$

respektivno, gde i označava indeks pristupa ($i = 1, 2$), a R_{ci} je realni deo impedanse Z_{ci} . Priraštaj koeficijenta transmisije definisan je sa [7]

$$\Delta s_{21} = \frac{\Delta b_2}{a_1} = \frac{b_2 - b_2^0}{a_1}, \quad (13)$$

gde su b_2 i b_2^0 kompleksni intenziteti reflektovanih talasa u prisustvu i odsustvu rasejača, redom, a Δb_2 njihova razlika. Odgovarajući scenario prikazan je na slici 5.

Na osnovu (12), priraštaj kompleksnog intenziteta reflektovanog talasa na pristupu druge antene je

$$\Delta b_2 = \frac{\Delta U_2 - \Delta I_2 Z_{c2}^*}{2\sqrt{R_{c2}}}, \quad (14)$$

pri čemu je

$$\Delta U_2 = -\Delta I_2 Z_{c2}. \quad (15)$$

Kada se (15) zameni u (14), dobija se

$$\Delta b_2 = \frac{-\Delta I_2 Z_{c2} - \Delta I_2 Z_{c2}^*}{2\sqrt{R_{c2}}} = \frac{\Delta U_2 \sqrt{R_{c2}}}{Z_{c2}}, \quad (16)$$

gde je

$$\Delta U_2 = \int_3^4 \mathbf{E}_s^1 \cdot d\mathbf{l}. \quad (17)$$

Da bismo odredili ΔU_2 , primenjujemo teoremu reciprociteta. U tu svrhu, zamenjujemo realni naponski generator ekvivalentnim strujnim generatorom koji je prikazan u donjem levom uglu slike 4. Ekvivalentan sistem prikazan je na slici 5. U obrnutom scenariju koji je prikazan na slici 6, druga antena radi kao predajna, pri čemu je pobuđena strujnim generatorom struje E/Z_{c2} . Na sličan način kao u (7), dobija se

$$\Delta U_2 = -\frac{\int (\mathbf{E}_{inc}^2 \cdot \mathbf{J}_{eq}^1 - \mathbf{H}_{inc}^2 \cdot \mathbf{M}_{eq}^1) dv}{E/Z_{c2}}, \quad (18)$$

pri čemu se $(\mathbf{J}_{eq}^1, \mathbf{M}_{eq}^1)$ i $(\mathbf{E}_{inc}^2, \mathbf{H}_{inc}^2)$ određuju iz scenarija prikazanih na slikama 5 i 6, redom. Kada se (16) i (18) uvrste u (13), sledi

$$\Delta s_{21} = -\frac{\int (\mathbf{E}_{inc}^2 \cdot \mathbf{J}_{eq}^1 - \mathbf{H}_{inc}^2 \cdot \mathbf{M}_{eq}^1) dv}{a_1 \frac{E}{\sqrt{R_{c2}}}}. \quad (19)$$

Na osnovu (11), imamo da je

$$a_2 = \frac{U_2 + I_2 Z_{c2}}{2\sqrt{R_{c2}}} = \frac{E}{2\sqrt{R_{c2}}} \quad (20)$$

jer je

$$I_2 = \frac{E}{Z_{c2}} - \frac{U_2}{Z_{c2}}. \quad (21)$$

Konačno, kada se (20) zameni u (19), dobija se izraz za priraštaj koeficijenta transmisije:

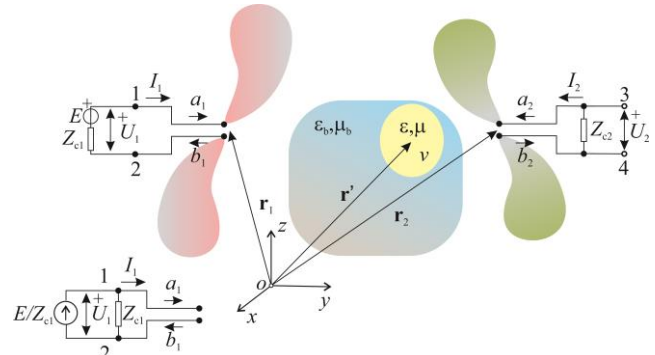
$$\Delta s_{21} = -\frac{\int (\mathbf{E}_{inc}^2 \cdot \mathbf{J}_{eq}^1 - \mathbf{H}_{inc}^2 \cdot \mathbf{M}_{eq}^1) dv}{2a_1 a_2}. \quad (22)$$

Na sličan način mogu se odrediti i priraštaji koeficijenata refleksije. Rezultati za priraštaje svih parametara rasejanja mogu se generalizovati za bilo koji par antena u mernom sistemu od M antena:

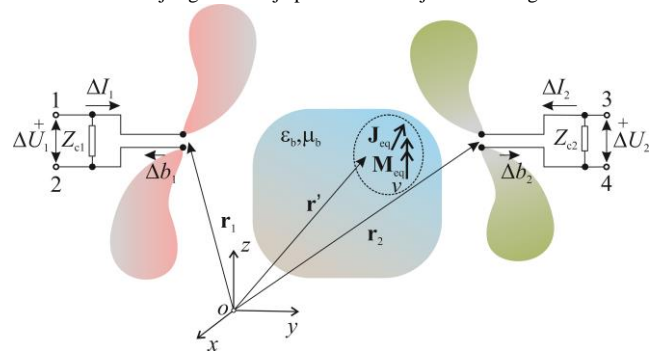
$$\Delta s_{ji} = -\frac{\int (\mathbf{E}_{inc}^j \cdot \mathbf{J}_{eq}^i - \mathbf{H}_{inc}^j \cdot \mathbf{M}_{eq}^i) dv}{2a_i a_j}, \quad i, j = 1, \dots, M. \quad (23)$$

III. ZAKLJUČAK

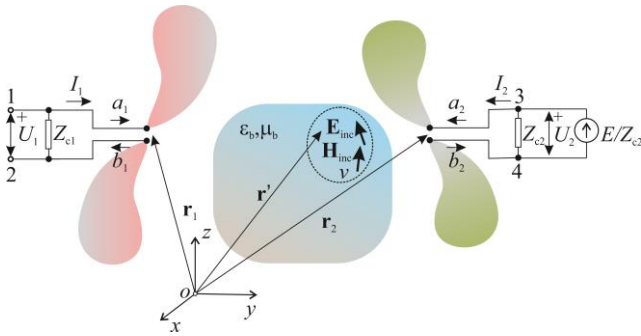
U ovom radu predstavljeno je izvođenje priraštaja bistatičke transfer funkcije (koeficijenta transmisije) između antena usled prisustva rasejača u proizvoljnoj linearnoj nehomogenoj sredini. Ova jednačina je fundamentalna za teoriju inverznog rasejanja i sastavni je deo većine algoritama za dobijanje slike pomoću mikrotalasa. Dobijeni izraz je opštiji od izraza u [9] i [10] jer se ne ograničava na nemagnetske sredine. Takođe, pokazano je da važi i u slučaju kada su nominalne impedanse pristupa kompleksne i različite.



Slika 4. Merna postavka za određivanje koeficijenta transmisije. Ekvivalentni strujni generator je prikazan u donjem levom uglu.



Slika 5. Ekvivalentni scenario za određivanje priraštaja s-parametara.



Slika 6. Teorema reciprociteta primenjena na scenario sa slike 5.

complex.

Generalization of transfer functions among antennas in inverse-scattering problems

Anja Kovačević, Marija Nikolić Stevanović i Antonije Đorđević

ZAHVALNICA

Sredstva za realizaciju ovog rada delimično su obezbedena od strane Ministarstva za obrazovanje, nauku i tehnološki razvoj Republike Srbije, Sporazumom o realizaciji i finansiranju naučnog rada Elektrotehničkog fakulteta u Beogradu (broj ugovora 1817/3), i od strane Srpske akademije nauka i umetnosti (projekat F133).

LITERATURA

- [1] M. Salucci, G. Oliveri, and A. Massa, "GPR prospecting through an inverse-scattering frequency-hopping multifocusing approach," *IEEE Transactions on Geoscience and Remote Sensing*, vol. 53, no. 12, pp. 6573-6592, Dec. 2015.
- [2] S. Sadeghi, K. Mohammadpour-Aghdam, R. Faraji-Dana, and R. J. Burkholder, "A DORT-uniform diffraction tomography algorithm for through-the-wall Imaging," *IEEE Transactions on Antennas and Propagation*, vol. 68, no. 4, pp. 3176-3183, April 2020.
- [3] L. Crocco, I. Karanasiou, M. James, R. Conceição, *Emerging Electromagnetic Technologies for Brain Diseases Diagnostics, Monitoring and Therapy*, Switzerland, Springer, 2016.
- [4] J F. Zidane *et al.*, "Nondestructive control of fruit quality via millimeter waves and classification techniques: investigations in the automated health monitoring of fruits," *IEEE Antennas and Propagation Magazine*, vol. 62, no. 5, pp. 43-54, Oct. 2020.
- [5] M. Pastorino, *Microwave Imaging*, Wiley, Hoboken, NJ, USA, 2010.
- [6] N. Nikolova, *Introduction to Microwave Imaging*, EuMA High Frequency Technologies Series, Cambridge University Press, Cambridge, 2017.
- [7] D. M. Pozar, *Microwave Engineering*, John Willy and Sons, USA, 2012, Section 4.1, pp. 166-173.
- [8] M. Haynes and M. Moghaddam, "Vector Green's function for S-parameter measurements of the electromagnetic volume integral equation," *IEEE Transactions on Antennas and Propagation*, vol. 60, no. 3, pp. 1400-1413, Mar. 2012.
- [9] A. S. Beaverstone, D. S. Shumakov, and N. K. Nikolova, "Frequency-domain integral equations of scattering for complex scalar responses," *IEEE Transactions on Microwave Theory and Techniques*, vol. 65, no. 4, pp. 1120-1132, April 2017.
- [10] M. Nikolic Stevanovic and A. Djordjevic, "Simple Derivation of Transfer Functions in Bistatic Scattering Model," accepted for publication in *IEEE Transactions on Antennas and Propagation*.
- [11] R. F. Harrington, *Time-Harmonic Electromagnetic Fields*, McGraw-Hill, New York, USA, 1961.
- [12] B. D. Popovic, "Electromagnetic field theorems", *Proc. IEE*, Pt. A, vol. 128, no. 1, 1981, pp. 47-63.

ABSTRACT

We derive the expressions for the increments of the scattering coefficients of an arbitrary antenna pair due the presence of the scatterer in a linear inhomogeneous medium. The main contribution of this work is the generalization of the expressions in the case when the medium in which the scatterer is located has magnetic properties. It was also shown that the same expressions are valid in the case when the nominal impedances of the ports are different and